(Univ. Prof. Dr. Friedrich Aumayr)

TECHNISCHE UNIVERSITÄT WIEN
Vienna University of Technology

Diplomarbeit

Proton transfer reactions forming the isomers HCO^+ and HOC^+

Ausgeführt am Institut für
Angewandte Physik
der Technischen Universtität Wien

unter der Anleitung von
Univ. Prof. Dr. Friedrich Aumayr

und am Insitut für
Ionenphysik und Angewandte Physik
der Universtität Innsbruck

unter der Anleitung von
Univ. Prof. Dr. Roland Wester

durch

Martin Kainz

Matrikelnummer: 0826888
Burgstraße 6
6973 Höchst

Dezember 2014

(Martin Kainz)

This curious world we inhabit is more wonderful than convenient;
more beautiful than it is useful;
it is more to be admired and enjoyed than used.

-- *Thoreau* --

Abstract

In this thesis I report on the dynamical scattering properties of proton transfer reactions producing the isomers HCO^+ and HOC^+. The two investigated reactions are H_3^++CO→HCO^+/HOC^++H_2 and $HOCO^+$+CO→HCO^+/HOC^++CO_2. The first of these ion-molecule reactions is of great interest in astrochemistry because it involves one of the most abundant ions (trihydrogen cation), as well as the second-most common molecule (carbon monoxide) in the interstellar medium and circumstellar envelopes.

The first section of this thesis describes a summary of previous investigations of the two isomers, either astronomical observations, theoretical calculations or experimental studies. Furthermore the experimental setup applied for the gas phase study, consisting of a crossed beam machinery in combination with a velocity map imaging spectrometer, is described. In the second part I discuss the measurement results of the two reaction. The obtained 3D-velocity images show forward scattering for all investigated collision energies but a kinematic separation of both species is not possible. A fit for the internal energy distribution of the reactions is performed and an upper bound for the HOC^+/HOC^+ ratio is determined. The limiting factor for a separation of the two isomers appears to be the high internal excitation of the products. The thesis concludes with an outlook for the improvement concerning the ion-beam preparation, as well as further experimental plans.

Zusammenfassung

In dieser Arbeit berichte ich von dem dynamischen Streuverhalten von Protontransfer Reaktionen welche die Isomere HCO^+ and HOC^+ erzeugen. Die zwei untersuchten Reaktionen sind H_3^++CO→HCO^+/HOC^++H_2 und $HOCO^+$+CO→ HCO^+/HOC^++CO_2. Die erste dieser Ion-Molekül Reaktionen hat sehr großes Interesse in der Astrochemie, weil sie eines der häufigsten Ionen (dreiatomiges Wasserstoffkation) und das zweithäufigste Molekül (Kohlenstoffmonoxid) im interstellaren Medium und zirkumstellaren Hüllen beinhaltet.

Der erste Abschnitt der Arbeit beschreibt eine Zusammenfassung von vorhergehenden Untersuchungen von den zwei Isomeren. Diese Untersuchungen beinhalten astronomische Beobachtungen, theoretische Berechnungen und experimentelle Studien. Des Weiteren wird der experimentelle Aufbau, welcher für die Untersuchung der Gasphase verwendet wird, beschrieben. Das Aufbau kombiniert ein Kreuzstrahlexperiment und ein Velocity-Map-Imaging-Spektrometer. Im zweiten Teil werden die Messergebnisse der zwei untersuchten Reaktion diskutiert. Die ermittelten dreidimensionalen Geschwindigkeitsbilder zeigen eine Vorwärtsstreuung für alle untersuchten Kolissionenergien aber keine kinetische Trennung der zwei Isomere. Ein Fit für die Verteilung der internen Energie wird vorgestellt, mit welchem eine obere Schranke für das HOC^+/HOC^+ Verhältnis bestimmt werden kann. Der limitierende Faktor für eine gute Trennung der zwei unterschiedlichen Isomere ist die hohe interne Anregung der Produkte. Abschließend wird ein Ausblick für Verbesserungen der Ionenstrahlerzeugung präsentiert und weitere mögliche experimentelle Untersuchungen werden vorgestellt.

Contents

Chapter 1

Introduction

In the last decades astrochemistry has emerged as a very important branch of natural science towards understanding the chemical composition of the universe. Over the past 40 years, astronomers have discovered a large number of molecules in the gas phase of space. These molecules are located in planetary atmospheres, star-forming regions and between stars, the so called interstellar medium (ISM). Denser regions are called interstellar clouds and consist of matter including gas in ionic, atomic, and molecular form, dust and cosmic ray [1]. The gaseous molecules are synthesized from precursor atomic material, which derives from the mass loss of previous destructions of stars. Several models exist that predict the synthetic paths connecting primary simple species with astronomically detected complex organic molecules [2]. In the last years the importance in astrochemistry has increased, as can especially be seen in the installation of ALMA[1] what has been fully operational in March 2013. In 2009 Roueff & Herbst presented a list of 133 neutral molecules and 17 molecular ions so far detected in circumstellar envelopes [3]. The great diversity of the observed molecules in the ISM is produced by many radiative and chemical processes [2]. One of the most important astrochemical processes is the ion-molecule reaction type, due to the high reactivity of ionic species. These reactions show an important influence, as they can explain the observed chemical composition in molecular clouds, circumstellar envelopes and planetary atmospheres [4–6]. For decades molecular ions have been conceived as progenitors of neutral molecules. In the last years the idea of dust grain processes, like in cometary ices, being the origin of com-

[1] ALMA is the acronym for Atacama Large Millimeter/submillimeter Array and is an astronomical interferometer of radio telescopes in the Atacama desert of norther Chile.

plex molecules observed in the ISM has found a lot of interest [7, 8]. The most current discussion regards the formation of polycyclic aromatic hydrocarbons [9]. However, gas phase ion-molecule reactions are still a crucial process for astrochemical models in order to explain the composition of molecular species in the ISM.

The most abundant molecules in the ISM are molecular hydrogen (H_2) and carbon monoxide (CO), whereas the most abundant molecular ions for the evolution of interstellar molecular clouds are the trihydrogen cation (H_3^+) and protonated carbon monoxide (HCO^+). H_3^+ is stable in the ISM due to the low temperature and low density of interstellar space. This ion was detected for the first time in 1913 by Thomson when he studied the resultant species of plasma discharge [10]. In 1925 Hogness & Lunn discovered the formation pathway of H_3^+. Their investigations on hydrogen discharge have shown that by increasing the pressure of molecular hydrogen, the amount of H_3^+ increases linearly and the amount of H_2^+ decreases [11]. This behaviour suggested the proton exchange formation pathway

$$H_2^+ + H_2 \rightarrow H_3^+ + H\,. \tag{1.1}$$

In the ISM H_2^+ is produced manly by cosmic ray ionization of molecular hydrogen

$$H_2 + c.r. \rightarrow {H_2}^+ + e^- + c.r.\,. \tag{1.2}$$

Martin and coworkers suggested that H_3^+ may be present in the interstellar space, due to the large amount of hydrogen and its exothermic reaction pathway ($\sim 1.5\,\mathrm{eV}$) [12]. Further studies suggested the importance of H_3^+ for the formation of many observed molecular ions [13]. In 1996 the first H_3^+ was detected in the ISM by Geballe & Oka in two molecular interstellar clouds in the sightlines GL2136 and W33A [14]. The H_3^+ destruction is mostly controlled due to reactions with neutrals, mainly CO, and by recombination reactions [15]. The reaction with CO forms the stable formyl cation HCO^+ and the metastable isoformyl cation HOC^+. This molecular ion (HCO^+) was first detected by Buhl & Snyder and is the most abundant molecular ion in the ISM after H_3^+ [16].

Until now, the models of the reaction networks in the ISM rely heavily on theoretical calculations, as the study of ion-molecule reactions under ISM conditions is experimentally very challenging due to the low temperature and density requirement. In previous experimental investigations classical techniques such

as the afterglow method or the flow tube arrangement were used [17]. Another technique is ion trapping in cryogenic radio frequency multipole ion traps [18]. These experimental studies do not yield dynamical information about the reactive processes. Such informations are how the reactants approach each other, which spatial constraints appear or how transition states influence the redistribution of the collision energy.

Since HCO^+ has been detected in the interstellar medium, the interest in this molecular ion and its isomer HOC^+ has remained. Rate coefficients are calculated [19–22] and the ratio of the two isomers is obtained by measurements [23–25]. The formation of the isomers as well as the isomerisation from the metastable HOC^+ to the stable HCO^+ is of interest [26, 27]. Many astronomers, chemists and physicist have investigated the ratio of HCO^+ and HOC^+ and observed variable values in different regions. Until now, it is still not clear which effects really influence the ratio of different regions in the ISM. The formation of aldehydes and alcohols in interstellar clouds depends on the ratio of the two cation isomers, where HCO^+ initiates aldehydes (e.g. formic acid CH_2O_2)[1] and HOC^+ initiates more likely a reaction chain leading to alcohols (e.g. methanol CH_3OH)[1] [28–31]. Thus, it is quite interesting to know more about the reaction dynamics which lead to these two isomers and the ratio of those.

The aim of my master thesis is to understand the dynamics of the most important reaction

$$H_3^+ + CO \rightarrow HCO^+/HOC^+ + H_2 \tag{1.3}$$

which leads to the formyl and isoformyl ions HCO^+ and HOC^+ in the ISM. A secondary reaction is investigated in this thesis, in which protonated carbon dioxide ($HOCO^+$) reacts with carbon monoxide

$$HOCO^+ + CO \rightarrow HCO^+/HOC^+ + CO_2 \tag{1.4}$$

and forms the same products as in the previous reaction. Beside reaction (1.3) this process also influence the ratio of the two isomers in the ISM a little. For this purpose a combined crossed beam imaging technique [32] is used to perform a

[1] CH_2O_2: 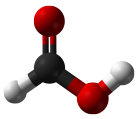 CH_3OH: 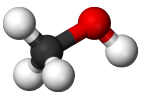

gas phase collision experiment at low relative energies. In these gas phase studies the energy and angular distribution of the reaction products are monitored as a function of the relative kinetic energy of the two reactants. Additionally the branching ratio of the two isomers HCO^+ and HOC^+ is analysed in terms of the relative energy. Due to the different enthalpies of the two reaction channels the isomers have different energies after the collision. We present a discussion of higher and lower limits for the ratio of the two isomers formed in the proton transfer reactions depending on the collision energy of the products.

In the following chapter I will first present previous investigations for the HCO^+/HOC^+ ratio, both theoretical and experimental studies. Afterwards an overview of the experimental setup and the velocity map imaging spectrometer is shown followed by the presentation of the experimental results. At the end of my thesis an outlook will be provided which command on further investigation and possible experimental plans.

Chapter 2

Previous studies on the HCO^+/HOC^+ ratio

In the last decades many astrochemists and astrophysicists were investigating in the formyl HCO^+ cation and the isoformyl HOC^+ cation. In this chapter an overview of the most important astronomical observations, theoretical calculations and experimental studies regarding the isomer ratio is presented.

2.1 Astronomical observations

One of the most important discoveries in molecular astrophysics is the detection of HCO^+ [16]. When Buhl and Synder were searching for HCN and its molecular isotope $H^{13}CN$ they discovered a new molecular line in Orion A and referred to it as the X-ogen line. The frequency determined for this X-ogen line was 89.190 GHz. Klemperer and coworkers suggested this line to be a HCO^+ transition frequency [33]. The presence of this molecular ion in the ISM validated chemical models which considered ion-molecule mechanisms as the dominant synthetic scheme. Further more they showed that most of the compounds found in the dense ISM are synthesized through ion-molecule reactions [34].

In 1983 Woods and coworkers made a sensitive search for the $J = 1 \rightarrow 0$ transition of HOC^+ in 14 interstellar sources and detected it towards Sgr B2 (Sagittarius B2) [24]. In this giant molecular cloud a lower limit for the isomeric abundance ratio HCO^+/HOC^+ of approximately 375 was yielded. For other interstellar sources they obtained lower limits between 75 and 510. They ex-

plained the gas phase ion-molecule reaction is the reason for the large isomeric ratio. Specifically, they suggested that both isomers are formed at the same rate via the reaction between CO and H_3^+

$$H_3^+ + CO \rightarrow HCO^+/HOC^+ + H_2\,. \tag{2.1}$$

While the metastable HOC^+ isomer is destroyed fast by reaction with atomic hydrogen, HCO^+ is destroyed more slowly by recombination with electrons [35].

Ziurys and coworkers repeated in 1995 the observations of the HCO^+ isomer towards Sgr B2(OH) and Orion-KL (Kleinmann-Low nebula), which is the most active part of the Orion Nebula and they detected the $J = 2 \rightarrow 1$ and $J = 3 \rightarrow 2$ lines of the HOC^+ ion for the first time. For a better estimation of the HCO^+/HOC^+ ratio they measured the lines of the ^{13}C and ^{18}O isotopomers of HCO^+. For Sgr B2(OH) they obtained a HCO^+/HOC^+ ratio of 140 - 360 and towards Orion-KL a ratio of ~ 1800 was estimated. Consequentially it was claimed that HOC^+ must exist in gas with $n(H_2) \sim 10^6\,cm^{-3}$ for $T \sim 80\,K$ [36].

Apponi and coworkers extended the observations for several star-forming regions and a few sources with known photo dissociation regions (PDR). They detected the $J = 1 \rightarrow 0$ transition in all sources except of one and in several of these clouds also the $J = 2 \rightarrow 1$ and $J = 3 \rightarrow 2$ transitions. For Sgr B2(OH) the same ratio was obtained and for the other investigated clouds they determined HCO^+/HOC^+ ratios typically in the range of 900 to 6 000[1]. From their observations of the widespread distribution of HOC^+ they could conclude that these ions are preferentially produced in PDRs [25].

More recent observations show absorption lines of HOC^+ from local diffuse and translucent clouds. For these clouds[2] a column density ratio HCO^+/HOC^+ of 70 - 120 could be determined, which is a factor 5 - 50 lower than typically found in dense dark gas, but comparable to observations in dense PDRs [27].

HOC^+ and CO^+ have been detected towards two well-known PDRs, S140 and NGC 2023 by Savage and coworkers in 2004 [37]. This study predicts that the charge transfer reaction $H_2^+ + CO \rightarrow CO^+ + H_2$ is not the major source of the CO^+ cation, because of the scarcity of H_2^+. Formation from direct photoioniza-

[1] HCO^+/HOC^+ ratio for: DR21(OH) = 2 600, D34.3 = 4 000, L134N = 4 500, NGC2024 = 900, NGC7538 = 3 500, Orion(3N,1E) = 2 000, Orion-KL = 2 100, W3(OH) = 6 000, W51M = 1 300

[2] coordinates: B0355+508, B0415+379, B0528+134, B01730-130, B2200+420

tion of CO is not likely either in this environment, since its ionization potential is very high. The dominant reason is the reaction of C^+ with OH or O_2. The investigation for the ratio of HCO^+/HOC^+ yielded 12 400 for S140 and 1 913 for NGC 2023. Although neither NGC 2023 nor S140 shows a definitive enhancement of HOC^+ relative to HCO^+, there seems to be a correlation between HOC^+ and CO^+.
The astronomical observations show different ratios, which depend on the composition of the detected cloud. However, it is not clear which combination of cloud properties really influence the ratio.

2.2 Theoretical calculations

After the unidentified interstellar emission line (X-ogen) was reported in 1970, Klemperer calculated the $J = 1 \rightarrow 0$ transition frequency of the cation HCO^+ to be close (0.06% deviation) to the measured frequency [33]. HCO^+ was predicted to be an abundant ion in dense interstellar clouds by Herbst and coworkers. To prove that HCO^+ is the carrier of the X-ogen line, they estimated the $J = 1 \rightarrow 0$ transition in $H^{13}CO^+$ which was then observed in a number of X-ogen sources [23]. The transition line $J = 1 \rightarrow 0$ for HOC^+ was first calculated by Herbst & Klemperer. They argued that both isomers are formed at the same ratio and the metastable HOC^+ is rapidly destroyed by the reaction with atomic hydrogen

$$HOC^+ + H \rightarrow HCO^+ + H \tag{2.2}$$

while HCO^+ is depleted more slowly by recombination with electrons [35].

Dixon and Freeman predicted the HOC^+ formation to be less likely because the proton affinity of the carbon atom of CO is higher than of the oxygen atom. They calculated a binding energy difference for the HOC^+ and HCO^+ isomers of 1.62 ± 0.15 eV [38, 39]. A variety of calculations concerning the HCO^+/HOC^+ abundance ratio was published by DeFrees and coworkers [40]. They calculated the tunneling from HOC^+ to form HCO^+ and claimed this process to be very unlikely. In addition, they investigated the exothermic reaction of HOC^+ and molecular hydrogen

$$HOC^+ + H_2 \rightarrow HCO^+ + H_2 \tag{2.3}$$

which was calculated to have a high activation energy barrier. If this reaction occurs at a low but appreciable rate, the abundance HCO^+/HOC^+ ratio would be close to the observed value of 375. A second isomerisation, which influences the ratio of the isomers is $HOC^+ + CO \rightarrow HCO^+ + CO$ (with a rate coefficient of $5.0 \times 10^{-10}\,cm^3\,s^{-1}$), due to the high reactivity of HOC^+ in comparison to HCO^+.

Further investigations of reaction (2.3) by Jarrold and coworkers suggested the reaction to be so fast that only few HOC^+ should be found in the ISM [41]. In the same work they presented a potential energy surface (PES) for reaction (2.1). The energy barrier between the two weakly bound complexes $HCO^+ \cdots H_2$ and $HOC^+ \cdots H_2$ is $1\,kcal\,mol^{-1}$ below the zero-point energy of the reactants H_3^+ and CO. Together with the calculation for reaction (2.1), where they obtained a ratio for HOC^+ of 20%, they predicted the abundance ratio HCO^+/HOC^+ to be lower than 10 000 at typical cloud temperatures and densities of $n(H_2) \sim 10^5$ and claimed this ratio will increase with higher $n(H_2)$.

Herbst and Woon improved the PES calculation for reaction (2.3). They obtained for temperatures of 50 K and at times from $10^{4.5}$ to 10^5 yr with their newly computed rate for reaction (2.3) an abundance ratio HCO^+/HOC^+ of 1 500 - 4 000 depending on the gas densities. They yielded a similar ratio as the one measured by Ziurys and Apponi towards Orion-KL. Additionally they presented a temperature dependent rate coefficient in the range of 10 - 300 K for $HOC^+ + H_2$ which is less than $1 \times 10^{-11}\,cm^3\,s^{-1}$ at temperatures below 100 K [42, 43].

The following part summarises current papers to which I refer the main theoretical considerations and which show the continuous interest in this reaction. To obtain theoretical insight regarding the stability and formation dynamics of the interstellar ions HCO^+ and HOC^+, Li and coworkers calculate stationary points on the full nine-dimensional PES for the electronic ground state [19]. The results of a reduced five-dimensional PES for the two reactions are shown in Fig. 2.1, where one can see the higher energy release of the $H_2 \cdots HCO^+$ complex compared to the $H_2 \cdots HOC^+$ complex. As one can see in Fig. 2.2 they calculate an exothermicity of $40.427\,kcal\,mol^{-1}$ (1.753 eV) and $2.684\,kcal\,mol^{-1}$ (0.116 eV) for the $HCO^+ + CO$ and $HOC^+ + CO$ channels respectively. This leads to an energy difference of 1.636 eV. This is in good agreement with the difference of the proton affinity of CO on the carbon and oxygen side, respectively (1.62 ± 0.15 eV [38]). In a following work they also investigate reaction (2.1) in terms of intra-molecular

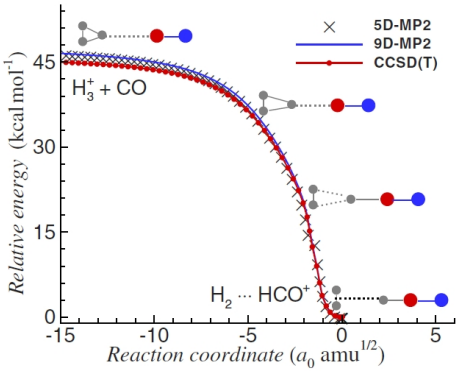

(a) MEP for the collinear H_3^++C→ $H_2 \cdots HCO^+$ reaction.

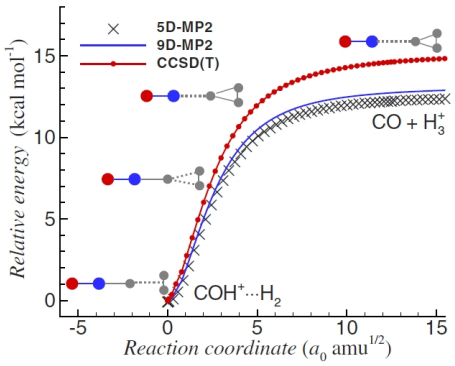

(b) MEP for the collinear H_3^++C→ $H_2 \cdots HOC^+$ reaction.

Figure 2.1: Minimum energy reaction paths (MEPs) of HCO^+ and HOC^+ (taken from [19]).

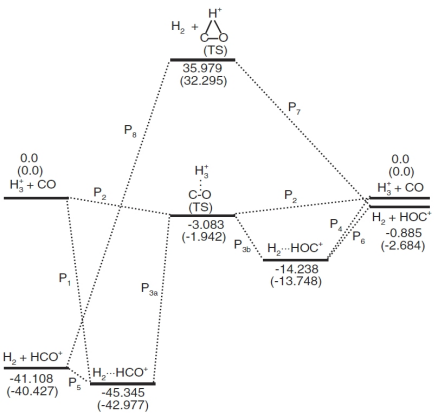

(a) Potential energy surface for the reaction H_3^++CO with the two transition states $CO \cdots H_3^+$ and $CO \cdots H^+$+H_2.

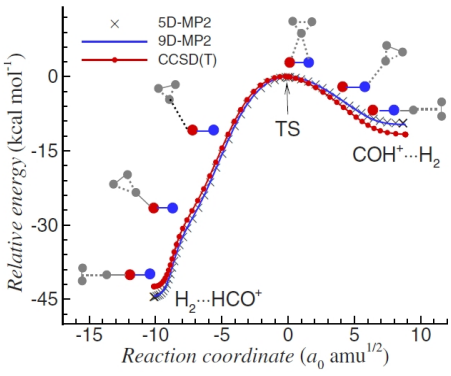

(b) Transistion state energy between the weakly bound complexes $HCO^+ \cdots H_2$ and $HOC^+ \cdots H_2$.

Figure 2.2: PES and transition state of the reaction H_3^++CO (taken from [19]).

vibrational energy redistribution (IVR) using direct dynamics calculations and obtain different excitations of the vibrational and bending modes of the products depending on the orientation of the CO molecule with respect to the collision axis. For the collinear approach at T = 20 K the bending mode ν(bend.) is not excited, whereas at T = 300 K or a 20°off-axis collision it is excited [44].

Thermal rate coefficients and product branching ratios in the temperature range of 20 K to 350 K are calculated by Yu in 2009 by using a direct ab initio molecular dynamics method [20]. For HCO^+ he obtains a constant thermal rate coefficient of $1.0\times10^{-9}\,cm^3\,s^{-1}$ over the whole temperature range. For the HOC^+ isomer the rate coefficient is $8\times10^{-11}\,cm^3 s^{-1}$ at T = 20 K and rises to $4.2\times10^{-10}\,cm^3\,s^{-1}$ at T = 350 K. He obtains a branching ratio HCO^+/HOC^+ to be $\sim$15.5 at T = 20 K and $\sim$2.5 at T = 350 K respectively.

Klippenstein and coworkers introduce calculated rate coefficients for reaction (2.1) with an ansatz for different interaction terms. The CO molecule has a small non-zero dipole moment, with the C atom slightly negative [45]. Thus, the charge-dipole interaction

$$V_{cd} = -\frac{dq}{R^2}\cos\theta \tag{2.4}$$

is the longest ranged term for the interaction of CO with H_3^+. However, the charge-quadropole

$$V_{cQ} = \frac{Qq}{4R^3}\left(3\cos^2\theta - 1\right) \tag{2.5}$$

and charge-induced-dipole interaction

$$V_{cid} = -\frac{q^2\left(\alpha_\parallel\cos^2\theta + \alpha_\perp\sin^2\theta\right)}{2R^4} \tag{2.6}$$

are of comparable magnitude. The charge-dipole and charge-quadrupole rate coefficients are proportional to $T^{-1/2}$ and $T^{-1/6}$, respectively, whereas the charge-induced-dipole capture is temperature independent [45]. Thus, as the temperature rises, both temperature dependent terms decrease. For the charge-quadrupole term, this decrease is quite gradual. The overall capture is not well-described by any single term over the whole temperature range [45]. In Fig. 2.3(a) the potential energy for the linear approach for H_3^++CO is shown for the different interactions and the sum of these. The thermal rate coefficient for this reaction is plotted in Fig. 2.3(b), where the sum of the interaction is compared with the QCISD(T)/CBS ab initio potential. Over the temperature range of 10 to

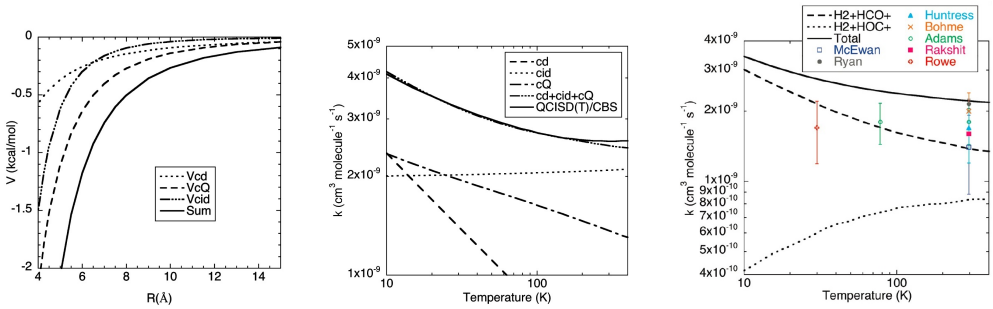

(a) Potential energy for the linear addition of H_3^+ to the C side of CO. The solid line denotes te sum of these three interactions.

(b) Temperature dependence of the calculated capture rate coefficient for H_3^++CO. The solid line denotes the QCISD(T)/CBS ab initio potential.

(c) Temperature depending rate coefficients for the prodcuts HCO^++H_2 and HOC^++H_2.

Figure 2.3: Potential energy and rate coefficient for H_3^++CO with charge-dipole(cd), charge-induced-dipole(cid) and charge-quadrupole(cQ) (taken from [45]).

400 K these two curves are almost identical, with a small difference of 5% at the highest temperatures. This increase is indicative of contributions from an additional term in the potential. Fig. 2.3(c) illustrates the rate coefficients for the two products HCO^+ and HOC^+. Over the 10 to 400 K temperature range, the predicted rate coefficient for HCO^+ is described by the modified Arrhenius expression[1] $k = 1.36\times10^{-9}(T/300)^{-0.142}\exp(3.41/T)\,cm^3\,s^{-1}$, while that for HOC^+ is $k = 8.49\times10^{-10}(T/300)^{0.0661}\exp(-5.21/T)\,cm^3\,s^{-1}$. Over this temperature range, all three terms have a strong influence on the rate coefficient. For temperatures of more than 500 K the simulated curve hints to an increase of the ratio for the HOC^+ isomer.

Le and coworkers evaluate the reaction cross sections and thermal rate coefficients for the production of HCO^+ and HOC^+ by using quasi-classical trajectory simulations [21]. In Fig. 2.4 the results are shown. For the reaction cross section one can see a decrease at higher collision energies and the cross section for a relative energy of 14 kJ mol^{-1} (0.14 eV) is $\sim$60 Å^2 for HCO^+ and $\sim$30 Å^2 for HOC^+, respectively. In the temperature range between 75 and 300 K the rate coefficients show a constant trend.

[1] $k = A(T/T_0)^n e^{-E_a/(RT)}$ with T_0 is a reference temperature and E_a is the activation energy.

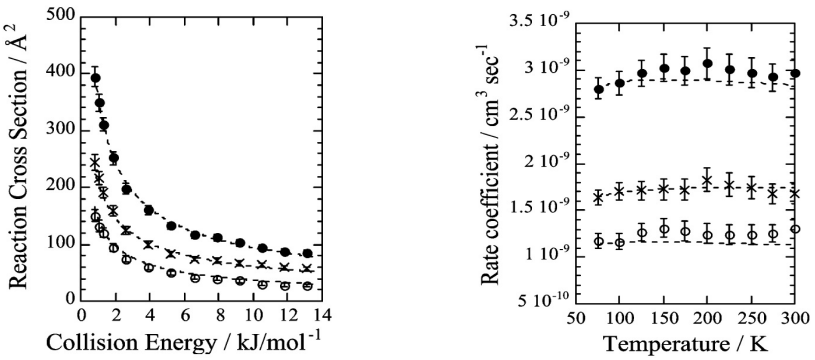

(a) The reaction cross section as a function of the relative translational energy of the H^+ and CO reactants.

(b) Thermal rate coefficients as a function of the temperature in canonical trajectory simulations.

Figure 2.4: Reaction cross section and rate coefficient for HCO^+(×), HOC^+(○) and both products (•) are shown (taken from [21]).

2.3 Experimental studies at low collision temperatures

After the X-ogen line was detected in 1970, Woods and coworkers observed the $J = 1 \rightarrow 0$ rotational transition of the HCO^+ ion. They used a discharge in various mixtures of hydrogen and carbon monoxide, cooled to ~ 80 K. They obtained an absorption at 89.188 GHz which is close to the X-ogen line (89.190 GHz) and defined this as the HCO^+ $J = 1 \rightarrow 0$ line [46].

In laboratory measurements Gudeman & Woods have assigned some of the lines in the spectrum from a discharge through a CO and H_2 mixture to HOC^+. The measured frequency was 89.487 GHz and they determined this to be the $J = 1 \rightarrow 0$ rotational transition line of the HOC^+ ion [47]. In the same year Illies and coworkers studied the collision-induced dissociation with H_3^+ and CO at 300 K [48]. By measuring the C^+/CH^+ ratio to be 1.49 and comparing it to electron impact reactions of different molecules (CH−2D and CD_3OH) they estimated the product to be predominantly HCO^+. However, their data indicates that a small amount of HOC^+ is also produced with a probability of $\sim 6\%$. If HOC^+ is depleted at the same rate as HCO^+ by the recombination with electrons, these experimental results would lead to an interstellar HCO^+/HOC^+ abundance ratio of almost 16, which is far below the observed value of 330. Thus, Jarrold suggested the result determined by Illies and coworkers probably

represents only a lower limit [41].

The HOC^+ isomer and its depletion in a selected-ion flow tube was investigated by Freeman and coworkers [39]. For this they used different methods to produce the HOC^+ ions and used H_2 and CO as a specified neutral reactant. A rate coefficient of $0.47\times10^{-9}\,cm^3\,s^{-1}$ for H_2 and of $0.86\times10^{-9}\,cm^3\,s^{-1}$ for CO, respectively, was determined.

As the isomerisation from HOC^+ to the stable HCO^+ is very important for the ratio of these two isomers the isomerisation rate of reaction (2.3) at 25 K was investigated by Smith and coworkers by using a temperature variable 22-pole ion-trap apparatus [26]. Mass-selected CO^+ ions are injected from a storage ion source into the cooled ion trap, where they are stored in the presence of H_2 for varying trapping times. During this time, the CO^+ is rapidly converted to the two isomers HCO^+ and HOC^+. The isomerisation according to reaction (2.3) is a competition to the accumulation of reaction (2.1) forming HOC^+. For determining the abundance of the isomers as a function of time, the method of chemical probing has been applied. Laboratory measurements by McEwan indicated that reaction (2.3) is relatively fast ($k \sim 10^{-10}\,cm^3\,s^{-1}$) at 300 K [49], what is a good explanation for the high ratio of HCO^+ in conditions where much molecular hydrogen exists.

In 2002 Wester and coworkers used the technique of foil-induced Coulomb explosion imaging (CEI) combined with a heavy ion test storage ring (TSR) to investigate in the relaxation dynamics of deuterated formyl and isoformyl cations (DCO^+ and DOC^+) [50]. Their experimental results indicate a constant abundance of DOC^+ molecules in the stored ion beam of about 10% for storage times of a few milliseconds up to some seconds.

The proton transfer reaction forming the formyl cation HCO^+ and the metastable isoformyl cation HOC^+ was studied by many physicists in the last years and still shows a remaining interest. The main part of the investigations of this reaction were theoretical calculations and only a few experimental studies were done. To get more insight into this reaction and especially the ratio of the two isomers, we will use a crossed beam apparatus in combination with a velocity map imaging spectrometer to study the dynamical properties of this reaction. In the following chapter the used experimental setup and the velocity map imaging detection will be described.

Chapter 3

Methods

Crossed beam scattering experiments are often used to study atomic and molecular dynamics. Two reactant beams collide in a small interaction volume where the reactants are cooled either due to supersonic expansion or by collisions with a cold buffer gas in the ion trap. With such a setup, collision processes at low relative energies can be studied. To detect the product ions and obtain information about the reaction dynamics, velocity map imaging has established itself in the last years as a very useful method. This technique has been introduced by Eppink and Parker [51]. The advantage of this technique is based on the possibility to map the velocity distribution of the products onto a detector with a high accuracy.

3.1 Experimental setup

In the group of Professor Roland Wester in Innsbruck, an experimental setup has been developed to study low energy reactive collisions between ion an neutral beams. The setup combines a crossed beam machinery with a velocity map imaging spectrometer (VMI). The experiment is controlled by two pulse generators at a frequency of 20 Hz. In Fig. 3.1 the most important components are shown. In the following chapter I will briefly describe the different sectors. A very detailed description of the setup has already been given in many papers and theses [52–56].

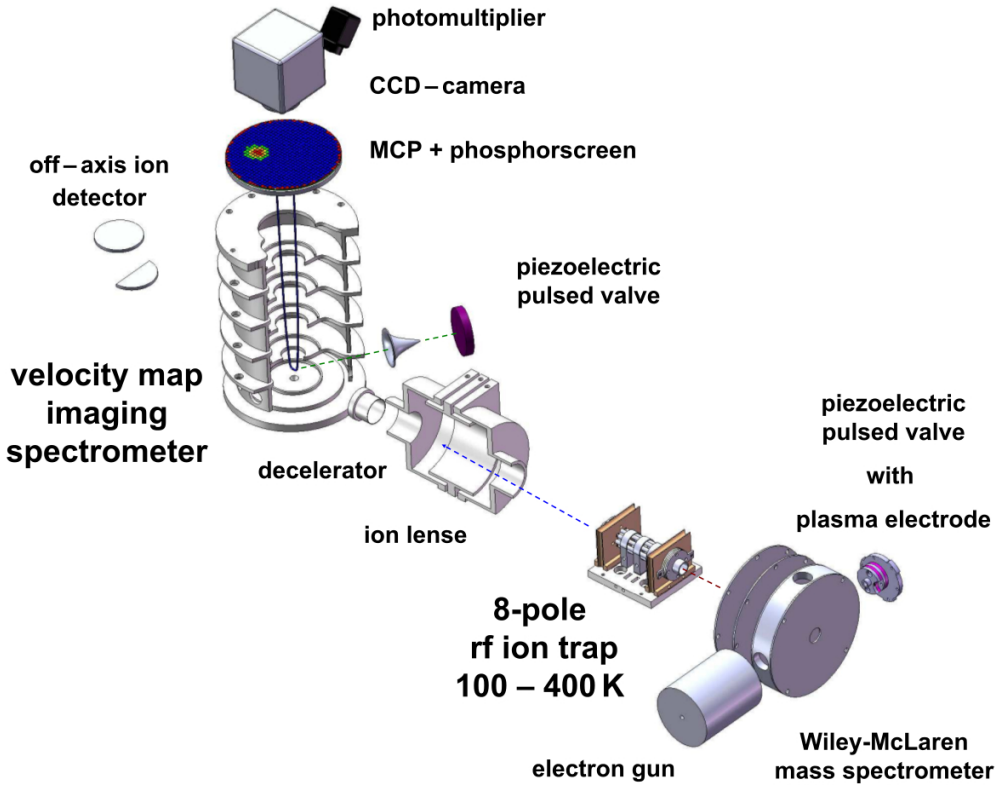

Figure 3.1: Setup of the experiment: The combination of a crossed beam setup and a velocity map imaging (VMI) spectrometer offers the possibility to carry out crossed molecular beam studies. The multipole trap enables the study of internally cold ions. The ions are generated in the source chamber using plasma discharge. These ions are accelerated via a Wiley-McLaren mass spectrometer using a field gradient. In the 8-pole radio frequency ion trap the ions are stored and afterwards they are extracted and focused into the centre of the scattering chamber, where they collide with a supersonic neutral beam. With the VMI spectrometer the product ions are detected on a micro-channel plate (MCP) and a phosphor screen and imaged with a CCD-camera. By using a photomultiplier the time of the impact at the MCP can be measured. This experiment is pulsed at a repetition rate of 20 Hz (Graphic taken from [52]).

3.1.1 Ion beam generation

As discribed in the previous section two different ions (H_3^+ and $HOCO^+$) are used in the experiment. The method to produce the ions depends on the produced species, in our case trihydrogen cations H_3^+ and the protonated carbon dioxide $HOCO^+$. In both cases trihydrogen cations are created in the ion source (see Fig. 3.2). For using H_3^+ as product ions they can be extracted directly from the ion source. To create the $HOCO^+$ ions, H_3^+ cations have to collide in the ion trap with carbon dioxide.

The trihydrogen cations are created by a pulsed supersonic expansion in a plasma ion source. The supersonic gas jet is created by using a home-built piezo electric valve. The used gas is molecular hydrogen (H_2) and the pressure of the gas before the piezo valve ranges from 0.8 to 1.5 bar. The gas is then expanded into the vacuum chamber with a pressure of around 1×10^{-5} mbar. A ring electrode is located at a distance of 2 mm after the nozzle of the piezo valve. This electrode is switched to a voltage of 800 - 1000 V for a time of typically 80 - 100 μs to ignite a plasma in the gas which is passing through it. To optimize the starting time and the duration of the plasma, a 10 kΩ resistor restricts a current over the ring electrode once the plasma starts. By monitoring the voltage over the resistor, the length of the gas pulse can be characterized.

In the plasma positive and negative hydrogen ions are produced. To mass select these ions a Wiley-McLaren time-of-flight mass spectrometer [57] is used and the ions are detected on a micro-channel plate detector (MCP) located off-axis at the end of the machine. The Wiley-McLaren mass spectrometer consists of four plates, switched to 228 V, 225 V, 214 V and 0V respectively, creating a field gradient to accelerate the ions. By changing the timing of the plasma pulse after the extracting of the supersonic beam and changing the extracting time of the Wiley-McLaren mass spectrometer the signal of the H_3^+ ions can be optimized. In Fig. 3.3 the intensity of the different hydrogen cations and the arrival time at the off-axis MCP is shown.

The time of flight (t_{TOF}) is inversely proportional to the ion velocity and the kinetic energy is the same for all ions determined by the same extraction voltage

$$E = q \cdot U = \frac{m \cdot v^2}{2}\,, \tag{3.1}$$

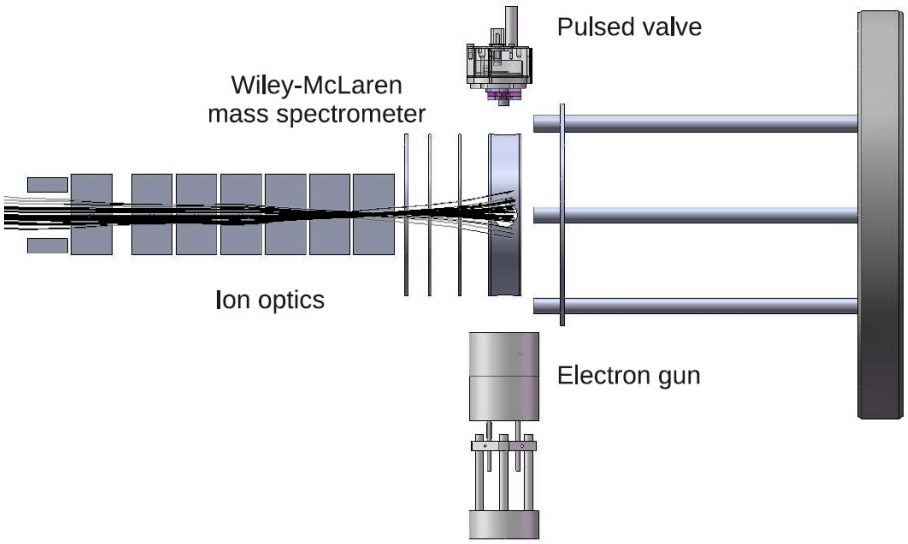

Figure 3.2: Schematic drawing of the ion beam source. A pulsed piezoelectric valve is used to creates a supersonic expansion. By using a plasma discharge, which can be stabilized by a pulse from an electron gun, the gas is ionized. To extract the ions towards the scattering region a Wiley-McLaren mass spectrometer is used. To focus and guide the beam six cylindrical lenses and deflector plates are used (graphic taken from [52]).

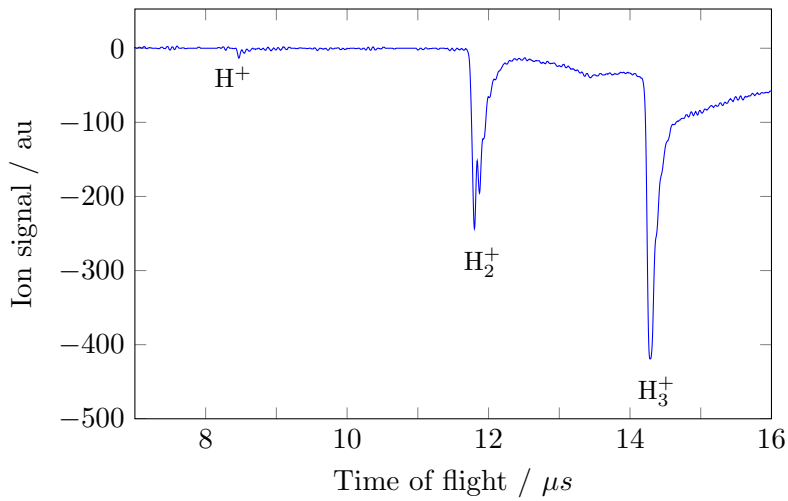

Figure 3.3: Ion signal: By changing the plasma delay and the extraction time of the Wiley-McLaren mass spectrometer the intensity of the different hydrogen cations can be optimized. The time of flight (t_{TOF}) relies on the mass of the ions.

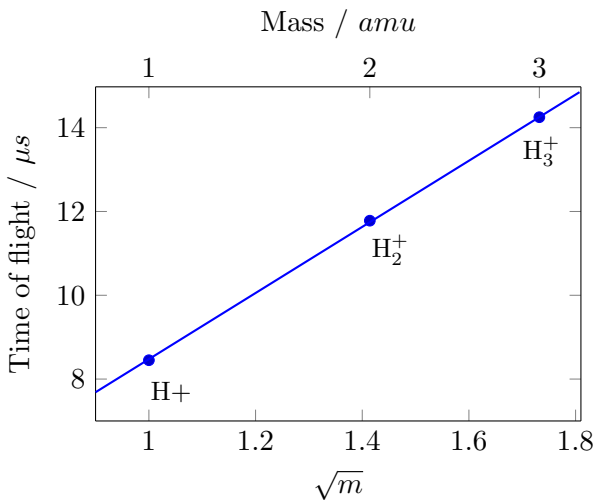

Figure 3.4: Time of flight of the three hydrogen cations H+, H_2^+ and H_3^+. One can see the proportionality $t_{TOF} \propto \sqrt{m}$.

so the TOF is directly proportional to the square root of the mass of the ion.

$$t_{TOF} \propto \sqrt{m} \tag{3.2}$$

This behaviour can be seen in Fig. 3.4, if one adds an additional time t_0 and multiplies $\sqrt{m}$ by a factor k.

$$t_{TOF} = t_0 + k\sqrt{m} \tag{3.3}$$

By doing a linear fit one gets $t_0 = 0.535\,\mu$s and k $= 7.93\,\mu\text{s}\,\text{amu}^{-1/2}$. After the three Wiley-McLaren (WiMC) electrodes an ion optical arrangement consisting of six cylindrical lenses is located to collimate the ion beam towards the scattering region. Before entering the radiofrequency octupole ion-trap the ions are guided using deflector plates positioned in horizontal and vertical directions.

3.1.2 Ion trap

To reduce the kinetic energy spread and cool possible excited vibrational modes, the ions are first stored in a 8-pole radio frequency (rf) ion trap (see Fig. 3.5), before entering the scattering chamber. A detailed description of the 8-pole ion trap is given in [52].

The effective potential for an ideal cylindrical multipole of the order n can be expressed as

$$V^*(r) = \frac{1}{4}\frac{n^2(qV_0)^2}{m\Omega^2 R_0^2}\left(\frac{r}{R_0}\right)^{2n-2} \tag{3.4}$$

where V_0 denotes the amplitude of the oscillating rf-field, m the mass and q the charge of a particle in an electric field oscillating on a frequency Ω in a trap with a inscribed diameter of $2R_0$. With a multipole order $n = 4$ the effective potential of the ion trap scales with $V_{eff} \sim r^6$. The total length of the trap is 36 mm and it consists of eight cylindrical rods with a diameter of $2r_0 = 2.5$ mm which are mounted into two copper side plates. The rods have an inscribed diameter of $2R_0 = 7.5$ mm. The geometry of the trap fulfils the relation

$$r_0 = \frac{R_0}{n-1} \tag{3.5}$$

to approximate a hyperbolic potential [18, 58]. A typical frequency of 8 MHz is applied with up to 150 V rf amplitude. The ions are stored in radial direction by the oscillating rf field of the rods. The endcaps of the trap (see Fig. 3.5) prevent the ions from leaving the trap. To manipulate the position of the ions during the storage time three static ring electrodes (shaping electrodes) surround the trap. These shaping electrodes shift the ions to one end of the trap. After opening the endcap located at the scattering chamber side the ions are accelerated from nearly the same region and therefore have a lower energy spread.

By closing the barrier at a specific time the ion trap can be used as a time-of-flight mass filter. So one can load the ion trap only with a given ion species. The whole ion trap can be set on an offset potential that matches nearly the kinetic energy, which the ions have after they were accelerated out of the ion source. Hence, approaching the potential of the trap decelerates the ions to 1 - 2 eV, and a short buffer gas pulse can be applied into the trap to further slow down the ions.

To extract the stored ions the endcap is switched from a repulsive potential to an attractive one. This potential gradient extracts the ions out of the ion trap and the ions leave the trap at the mean kinetic energy of its potential offset. To achieve a good energy resolution for the ion beam the gradient of the trap has to be optimized. This is done by changing the voltage of the endcaps and the shaping electrodes respectively. By using another pair of deflector plates and a

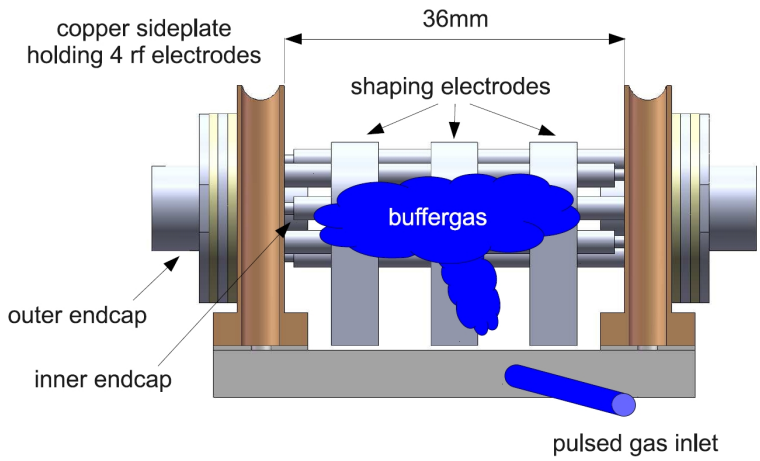

Figure 3.5: Sketch of the 8-pole ion trap. Instead of a buffer gas hydrogen is used on the one hand to cool the H_3^+ ions through inelastic collisions or the proton transfer reaction (3.6) and on the other hand carbon dioxide is used to produce $HOCO^+$ in the trap by collisions with H_3^+. The endcaps are used to load or unload the trap. Three shaping electrodes afford to shift the ions to one endcap to improve the energy spread after extracting the ions to the scattering chamber (graphic taken from [52]).

lens system these ions are guided towards the velocity map imaging spectrometer where they are decelerated to energies between 0.2 and 5 eV. The kinetic energy distribution of the ions is established by using the VMI spectrometer.

The generation of the two different species for the performed experiments (H_3^+ and $HOCO^+$) occurs in the ion trap.

H_3^+ generation

Stabilising the H_3^+ ions in the ion trap with Helium as buffer gas, as it is done in many other experiments, does not lead to an efficient capture of the ions in the trap. Using molecular hydrogen as buffer gas in the ion trap achieves the desired trapping. The method to use a buffer gas that is the same species than the trapped ion is used the first time in our setup and we assume that the incoming H_3^+ ions collide on the one hand elastic with the H_2 molecules. On the other hand a proton of the fast H_3^+ ion can transfer via a proton transfer reaction to the slow neutral H_2 ion.

$$H_{3\,(\mathrm{fast})}^+ + H_{2(\mathrm{slow})} \rightarrow H_{3\,(\mathrm{slow})}^+ + H_{2(\mathrm{fast})} \tag{3.6}$$

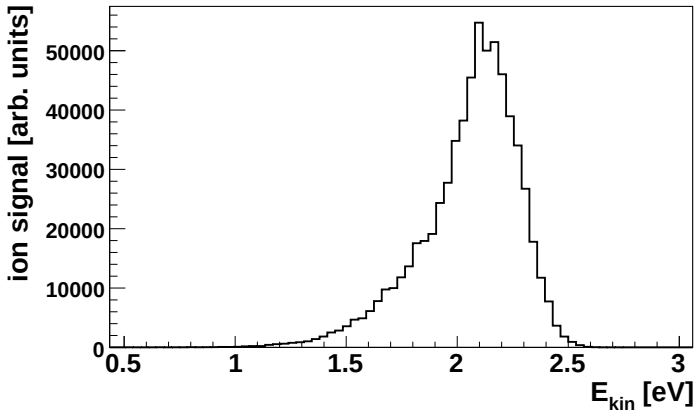

Figure 3.6: Nonthermal kinetic energy distribution of H_3^+ ions extracted from the ion trap and decelerated to 2.05 eV. An energy spread of $\Delta E = 222$ meV (RMS) can be obtained.

Both mechanisms cool down the H_3^+ ions and the energy spread of them can be reduced.

After the ions are extracted towards the scattering chamber their energy resolution is measured using the VMI setting of the spectrometer (see section 3.2.2). Fig. 3.6 shows a typically energy distribution of the H_3^+ ions. To improve the spatial distribution of the ion beam the SMI mode of the imaging spectrometer is used (see section 3.2.1).

$HOCO^+$ generation

In the second scattering experiment protonated carbon dioxide $HOCO^+$ collides with CO. To create the $HOCO^+$ ions two methods are tested. The first one is to create the ions directly in the plasma by adding a H_2/CO_2 mixture to the gas inlet. Due to the creation of CO_2^+ and $HOCO^+$ in the plasma, it is complicated to separate these two masses in the Wiley-McLaren mass spectrometer. Thus, the $HOCO^+$ cations are also produced in the ion trap by using CO_2 as buffer gas. H_3^+ ions are created in the same way as in the first experiment in the ion source. These H_3^+ ions collide in the ion trap with the CO_2 molecules and create via a proton transfer $HOCO^+$.

$$H_3^+ + CO_2 \rightarrow H_2 + HOCO^+ \tag{3.7}$$

3.1.3 Neutral beam source

The neutral molecules are generated by a pulsed supersonic beam. This beam originates from a second differentially pumped source chamber. A detailed description of the molecule source is given in [54]. A supersonic expansion is achieved when a highly pressurised (1 to 6 atm) gas is expanded through a small nozzle into vacuum [59]. To produce the supersonic beam a home-built piezoelectric valve is used. For the experiment carbon monoxide is expanded at 1 bar. Due to the low clustering effect of CO, no additional carrier gas has to be mixed. After the valve, the jet is skimmed using a 300 μm skimmer producing a supersonic expansion which cools the beam both rotationally and translationally. As can be seen from tabulated values for the heat capacities [60], at room temperature and below the vibrational mode of CO is essentially unexcited.

To measure the velocity distribution of the neutral beam the molecules are ionized via an electron impact process, using a 1 - 2 keV pulsed electron gun attached to the scattering chamber. The velocity of the neutral beam is measured in order to obtain the scattering parameters. By measuring the velocity spread of the beam its temperature can be obtained through $\sigma_v = \sqrt{k_B T/m}$. By using the VMI spectrometer the velocity distribution of the generated ions is detected. A jet velocity of 867 m/s with a sigma of 165 m/s is obtained as shown in Fig. 3.7(b). For our beam conditions we find a translational temperature of 91 K. Due to the momentum transfer by the electron impact, the temperature of the CO beam is increased and the value of 91 K is only a high upper limit for the beam temperature.

In order to maximize the scattering efficiency, by minimizing the overlap and interaction volume of the reactant beams, the spatial position of the neutral beam has to be determined. A smaller interaction volume produces less uncertainty in the mapping of the produced ions. To determine the position and the width of the molecular beam the imaging spectrometer is used in the spatially resolving mode (SMI mode - see chapter 3.2) to directly map the position of the beam. This technique is also used to optimize the placement of the piezo valve and to be sure that the expansion of the neutral beam is not conical but linear. A cut through the spatial distribution of the neutral beam is shown in Fig. 3.8. A beam diameter of 1.1 mm can be derived.

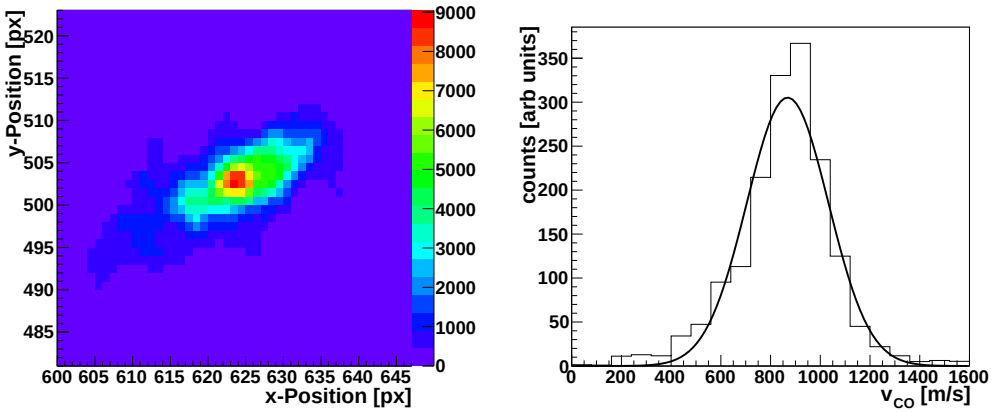

(a) Velocity map image(VMI) of the CO beam.

(b) A mean velocity of 867 m/s with a sigma of 165 m/s is measured for the molecular CO beam.

Figure 3.7: To define the velocity distribution of the molecular CO beam, the molecules are ionized using a pulsed electron gun. With the VMI settings of the spectrometer the velocity can be mapped onto the detector. For our conditions we measure a velocity of 867 m/s with a sigma of 165 m/s. With $\sigma_v = \sqrt{k_B T/m}$ a temperature of 91 K is obtained for the CO beam.

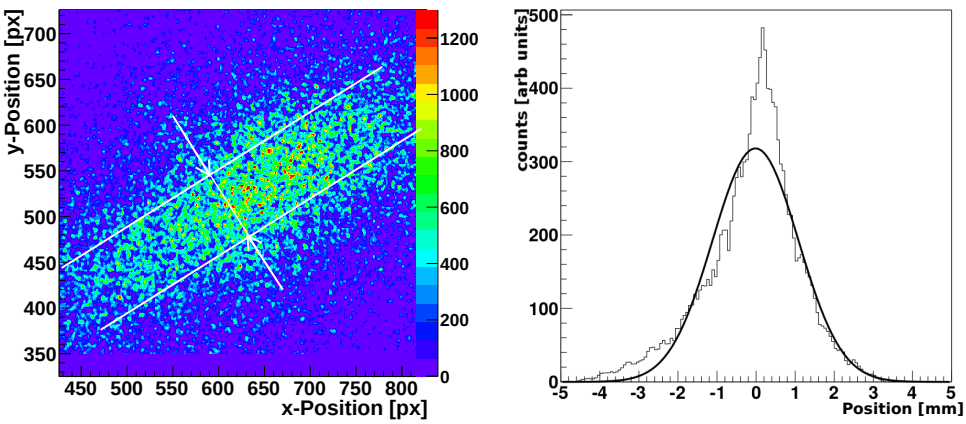

(a) Spatial map imaging (SMI) of the CO beam. The white lines in the picture shows the width of the beam.

(b) By transforming the picture of the CCD camera into the coordinates of the spectrometer a beam width of 1.1 mm can be assumed.

Figure 3.8: The position and the beam width of the CO beam is measured by using the spectrometer in the SMI mode (see chapter 3.2.1). To detect the neutral CO beam, it is ionized using a pulsed electron gun. The white lines in (a) show the width of the beam.

3.1.4 VMI spectrometer

The setup of the velocity map imaging spectrometer has been described in detail in many other publications [52–55, 61, 62]. Only a brief summary will be given here. To extract and focus the ions out of the scattering plane six cylindrical field plates (VMI 1 - VMI 6) are mounted onto each other. Between the two lowest plates the ion beam crosses the molecular beam. The lowest plate (VMI 1) acts as a repeller, whereas the sixth is grounded to generate a field free region between the imaging stack and the detector. To improve the resolution and minimize stray fields from the ion optics close to the imaging region the plates VMI 2 - VMI 6 are featured with a shielding. The shielding of the second plate features many cylindrical holes through which the molecular and ion beam can pass into the interaction region. These holes also provide the possibility to guide a second molecular beam or different lasers into the scattering region. In order to decelerate the incoming ions to a tunable kinetic energy, the first three plates of the VMI stack are held on a variable platform potential. Due to the low electrical field penetration of the voltage of the fourth plate, it can be assumed that it is sufficient to set only three plates on the platform voltage. This was tested by comparing the signal at the detector by setting only three plates on the platform voltage and setting as well the fourth plate on the same platform voltage. No difference in the imaging quality is observed.

After the incoming ion package has crossed the neutral molecular beam the field plates of the VMI stack are switched onto their working potential. This switching is usually done in 50 ns using fast commercial HV-switches (Behlke HTS 31). In order to provide a homogeneous field ramp for the extraction of the ions out of the interaction region it is necessary to synchronize the switching time for the different electrodes [54]. This is done using cable propagation delays giving a delay of the first three electrodes of 1 - 2 ns. After the electrodes are switched to the working potential the ions are accelerated towards a position and time sensitive detector system consisting of a double MCP in chevron configuration, a phosphor screen and a photomultiplier. If wished, the target mass can be isolated of other fragments by setting a time window for the voltage of the MCP. To detect the impact position on the detector a CCD-camera is used. The pixel density of the CCD is 11.75 px/mm, which has to be taken into account for transforming the impact position on the detector into a mm scale. A photomultiplier connected to a time-to-digital converter (TDC) is installed to

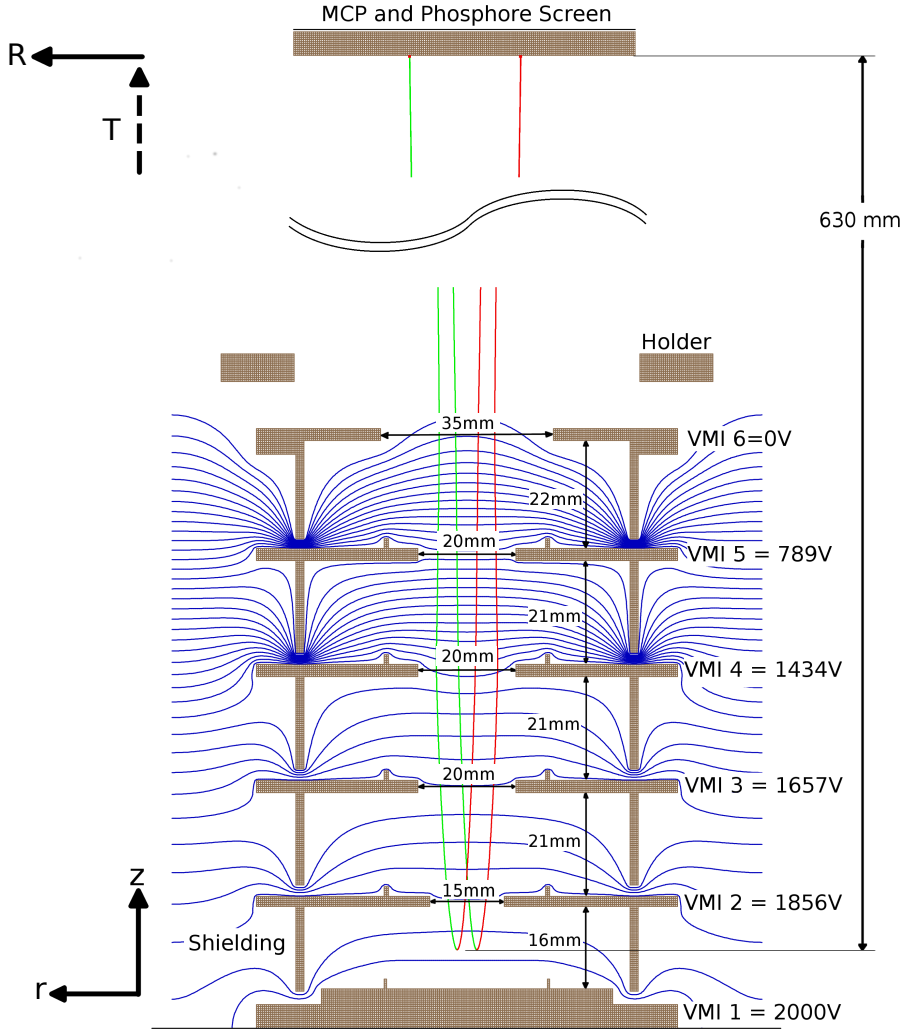

Figure 3.9: Schematic cut along a plane containing the symmetry axis of the setup with the voltages for the velocity map imaging (VMI) mode. The voltages for the 2-kV setting are: $U_1 = 2000\,\mathrm{V}$, $U_2 = 1856\,\mathrm{V}$, $U_3 = 1657\,\mathrm{V}$, $U_4 = 1434\,\mathrm{V}$, $U_5 = 789\,\mathrm{V}$ and $U_6 = 0\,\mathrm{V}$. The electrodes VMI 2 - VMI 6 feature a curtain-like shielding to avoid field distortions due to the close by electrodes outside the spectrometer. The distances between the electrodes and the size of the windows in the respective electrodes are displayed. The equipotential lines in blue with 100 V spacing as well as the ion-trajectories are calculated with SIMION [63].

determine the time of the impact of the produced ion [53]. To assure that the measured time of the TDC belongs to one defined particle, only events with one single detected ion are considered. Cycles with two or more events are discarded. By combining the velocity map imaging with the simultaneous detection of the flight time of each scattering event, a full three dimensional velocity distribution can be reconstructed. Compared with the time slice imaging method, where the detector is only switched on for a short time period to cut out the centre slice of the three dimensional velocity distribution, this method is capable to detect different ion species during the same measurement. The advantage of the slicing method is that the speed of the data acquisition can be enhanced, but the possibility to obtain a full three-dimensional velocity image is lost.

3.2 Collision process and detection

In this section the imaging process is given. A more detailed description of velocity map imaging and of spatial map imaging can be found in other published works [32, 64]. The following description allows us to understand how a specific imaging setup can be used to resolve different phase space properties, like its velocity or position. A particle with a defined mass, can be described by its starting properties (r, z, v_r, v_z, m) , where r is the horizontal position in the scattering region and z is the vertical position. v_r and v_z are the corresponding velocities in the respective directions. During the imaging process the mass of the ion can be treated as fixed and the symmetry of the apparatus is cylindrical. The ion imaging process can be described as a mapping of the vector $(r, z, v_r, v_z)_m$ onto the detector. Every event is described by the coordinates (R, T), where R is the radial position on the detector (using the CCD-camera) and T the time of flight (using the PMT + TDC setup described in this section) of the ion. The geometry and voltage of the imaging lens system define the transformation $(r, z, v_r, v_z)_m \rightarrow (R, T)$. The points of origin for r and R are located on the symmetry axis of the setup, whereas the origin of the z-direction is located between the first two electrostatic plates of the setup, 8 mm above the lowest one. The time of flight t_{TOF} is measured relative to the arrival time (T_0) of a particle at rest that is starting at $r = 0$ and $z = 0$.

To characterize the imaging resolution of the electric field configuration of the electrodes the radius R of the impact position and the arrival time t_{TOF} on the detector can be approximated in the first order as

$$R = (r, z, v_r, v_z) \begin{pmatrix} \frac{\partial R}{\partial r} \\ \frac{\partial R}{\partial z} \\ \frac{\partial R}{\partial v_r} \\ \frac{\partial R}{\partial v_z} \end{pmatrix}, \quad t_{TOF} = T_0 + (r, z, v_r, v_z) \begin{pmatrix} \frac{\partial T}{\partial r} \\ \frac{\partial T}{\partial z} \\ \frac{\partial T}{\partial v_r} \\ \frac{\partial T}{\partial v_z} \end{pmatrix}. \tag{3.8}$$

The time offset T_0 denotes the flight time of a particle from the centre of the VMI setup ($r = 0$, $z = 0$) with a zero initial velocity ($v_r = 0$, $v_z = 0$).

3.2.1 Spatial map imaging (SMI)

If the spatial position of the particle in the spectrometer is of interest, it can be mapped onto the detector

$$(r, z) \rightarrow (R, T). \tag{3.9}$$

By setting the voltages of the spectrometer to the required voltages this spatially resolving mode can be achieved. This mode is then called spatial map imaging (SMI) and is used as a tool for mapping and optimizing the shape of the ion beam and improving the overlap with the neutral beam. Additionally this technique can be used to monitor the spacial extension of the product ions. According to the investigation of [64], the voltages applied to the individual plates of the imaging spectrometer are $U_1 = 3000\,\mathrm{V}$, $U_2 = 2800\,\mathrm{V}$, $U_3 = 2600\,\mathrm{V}$, $U_4 = 1400\,\mathrm{V}$, $U_5 = 0\,\mathrm{V}$ and $U_6 = 0\,\mathrm{V}$ to obtain a SMI configuration. For the settings employed in the present experiment a scaling factor of

$$R = -3.1r \tag{3.10}$$

is simulated [52]. This mode provides a mapping in r and z. The scaling parameter is approximately one order of magnitude larger than the influence of respective velocity derivatives [64]. The negative magnification in equation (3.10) reflects that the spatial map imaging inverts the picture.

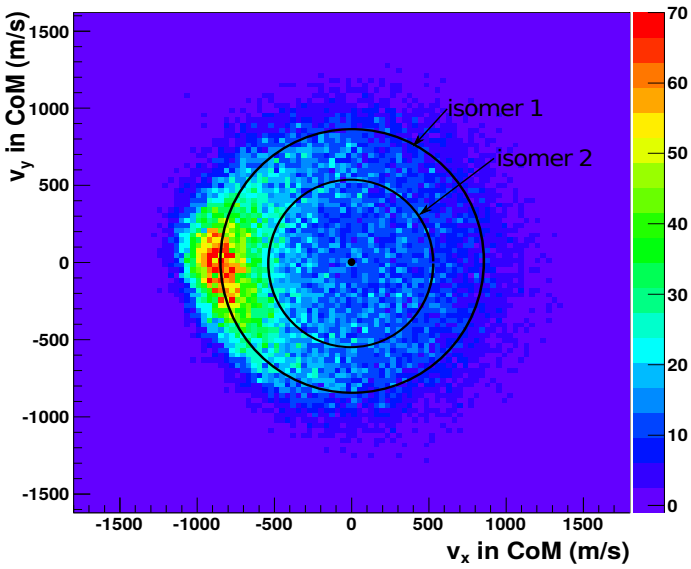

Figure 3.10: Velocity map image in the centre-of-mass frame. The two circles depict the velocity mean values of the two produced isomers.

3.2.2 Velocity map imaging (VMI)

The more interesting imaging mode, which can be achieved with the experimental setup, provides a mapping of the velocity of the particle onto the detector

$$(v_r, v_z) \rightarrow (R, T) \tag{3.11}$$

and is known as velocity map imaging (VMI). The VMI mode can almost be approximated in the first order to be independent of the spatial extension of the ion cloud which can be estimated to be about $(2\text{-}4\,\text{mm})^3$. This spatial extension can be estimated, when the produced ion cloud is extracted $1\text{-}2\,\mu$s after the collision of the ion package with the neutral beam. To increase the distance of the imaged HCO^+ and HOC^+ ions on the detector (see Fig. 3.10), the magnification of the spectrometer is adjusted to be maximal. This was simulated with SIMION to optimize the used detector area with the assumed velocities of the products and minimizing the aberrations of the spectrometer. The voltage settings for the velocity map imaging for this case are $U_1 = 2000\,\text{V}$, $U_2 = 1856\,\text{V}$, $U_3 = 1657\,\text{V}$, $U_4 = 1434\,\text{V}$, $U_5 = 789\,\text{V}$ and $U_6 = 0\,\text{V}$ (see Fig 3.9). These values are a fraction of the settings which were used in [32, 52]. To image the H_3^+ ions for measuring their energy distribution a different magnification

parameter is used. For this all voltages are scaled-up by the same factor of 1.5 to have the 3-kV settings. The flight time T_0 in the velocity map imaging mode (2-kV settings) for HCO^+ ions (m = 29 amu) starting at the centre of the setup is given by 7.2 μs. As an approximation the coordinates R and T only depend on v_r and v_z respectively [32]. This means that two ions with the same velocity and a different spatial initial position are detected onto the same spot on the detector. Most VMI experiments do not record the time of flight T, so the information of the velocity component v_z cannot be detected and only the information of the radial velocity v_r can be extracted. In ion-molecule reactions with a spherically symmetric velocity distribution, it is possible to reconstruct the initial velocity using an Abel inversion scheme [65] or it is possible to produced sliced images depending on the arrival time on the detector. In our experiment the time of flight of the ions is detected and so the velocity component v_z is observed. By knowing this additional velocity the radial velocity of the product ions is measured.

3.2.3 Calibration of the zero point of the detector

To determine the velocity origin of the detector, the scattering chamber is flooded with neutral argon gas which is then ionized with 1 keV electrons. Due to the fact that the velocity of the neutral gas in the scattering region is thermally distributed after some collisions with the chamber wall, the velocity image on the detector shows a homogeneous distribution. Thus, the origin (x_0, y_0) can be approximated to be (583.4 px , 480.4 px) (see Fig. 3.11).

3.2.4 Mapping simulation

As described in the beginning of this section the detection process of the product ion consists of a MCP in combination with a PMT. With these two detection methods a three dimensional velocity distribution can be measured. Assuming ideal velocity mapping, each position x, y of an ion detected on the detector corresponds to its laboratory velocity vector in the scattering region. With this projection, the velocity components v_x, v_y are easily calculated from the impact position using the equation

$$v_{x,y} = \frac{x, y - x_0, y_0}{M \cdot t_{TOF}} \tag{3.12}$$

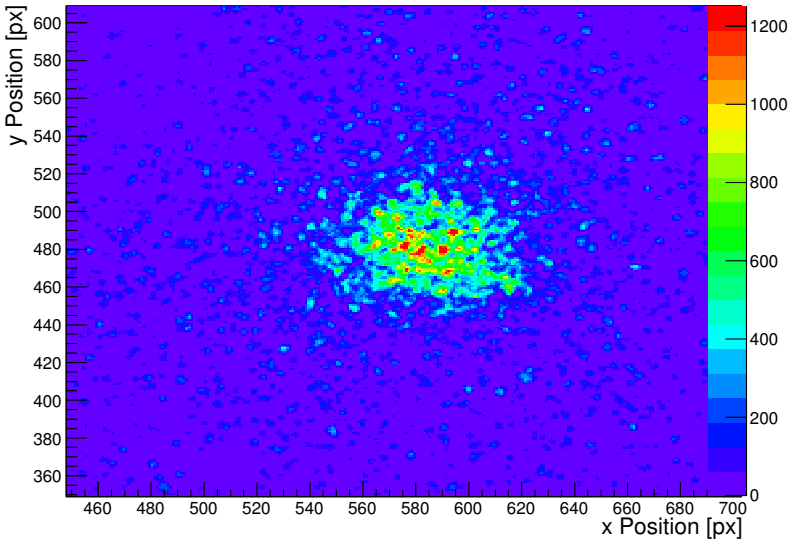

(a) VMI of the zero point.

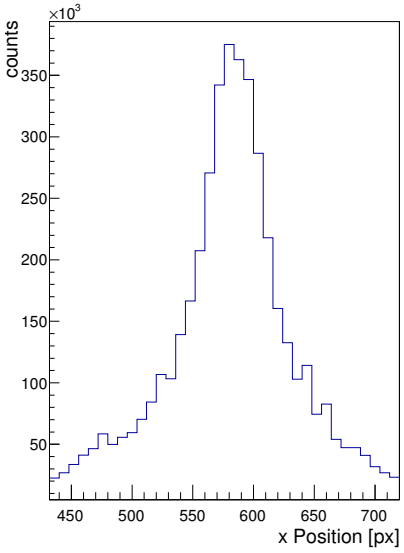

(b) Spatial distribution in the x-axis of the zero point measurement.

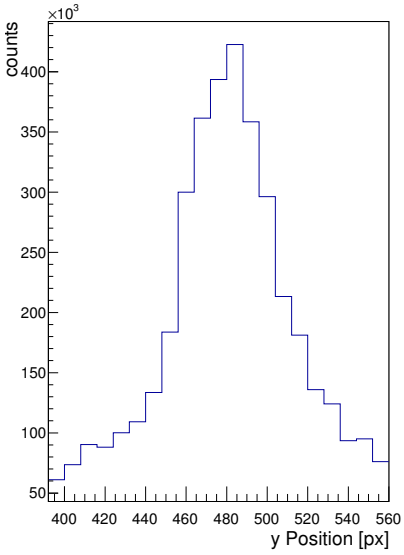

(c) Spatial distribution in the y-axis of the zero point measurement.

Figure 3.11: Measurement of the zero point of the detector. The scattering chamber is flooted with Ar gas which is then ionized using a 1 keV electron gun. Imaging the homogeneous velocity distribution lead to the zero point of the detector. The zero point is 583.4 pixel in x-direction an 480.4 pixel in y-direction.

where M denotes the magnification factor of the lens arrangement and t_{TOF} the time of flight to the detector. x_0, y_0 are the points of origin obtained from the zero velocity. The magnification factor M depends on the electric field gradient of the spectrometer [32] and is obtained from simulations of ion trajectories through the VMI spectrometer ran with SIMION [63]. By simulating the flight path of ions with a different starting velocity ($v_{x,y}$) out of the scattering region (see Fig. 3.12(c)) one can obtain the relation between this starting velocity and the impact position on the detector (see Fig. 3.12(a)). The straight line represents the magnification factor M, which is calculated to be 0.72. The magnification factor M is independent of the ion mass, so particles with the same velocity but unequal mass are detected at the same spot on the detector. The TOF however will depend on the ion mass. The value of t_{TOF} is identified by taking the results from the same SIMION simulation as described before.

The determination of the velocity component along the VMI spectrometer axis v_z is done in a slightly different way. For this, one takes the difference in the time of flight of the ion and a magnification factor M_t

$$v_z = \frac{T - T_0}{M_t} \,. \tag{3.13}$$

To identify the magnification factor M_t for the velocity in z-direction, another simulation of trajectories through the VMI spectrometers is performed with SIMION. By taking ions which a different starting velocity v_z and matching them with the arrival time T at the detector, obtains the magnification factor M_t, yielding a value of -35.6$\times 10^{-3}\,\mathrm{s}^2\,\mathrm{m}^{-1}$ (see Fig. 3.12(b)). This magnification factor represents $\frac{\partial T}{\partial v_z}$ and is negative due to the fact that ions starting with a positive velocity in z-direction arrive earlier at the detector. The time T_0 is the time for an ion starting out of the point of origin with $v_z = 0$. The data points in Fig 3.12 are simulated with a normal distribution ($\sigma = 1.1\,\mathrm{mm}$) for the starting position in the scattering region. This spatial spread leads to a distribution in the simulated velocities. Fig 3.12(a) and 3.12(b) present these error bars. In the case of the velocity in z-direction, the error due to the uncertainty in the spatial starting point are within the data points. The error bars in the x- and y-direction, increase with increasing velocities. This indicates the worse mapping of the VMI spectrometer for high velocities, because in this case the ions are nearly reaching the plates.

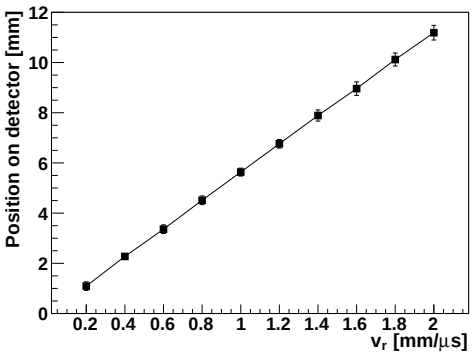

(a) Simulated position of the ion impact on the detector depending on the starting velocity $v_{x,y}$.

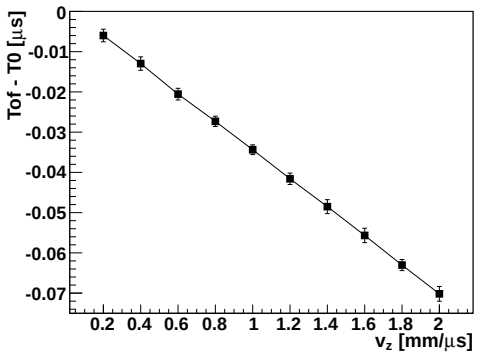

(b) Simultated difference from the flight time of the ion depending on the velocity v_z.

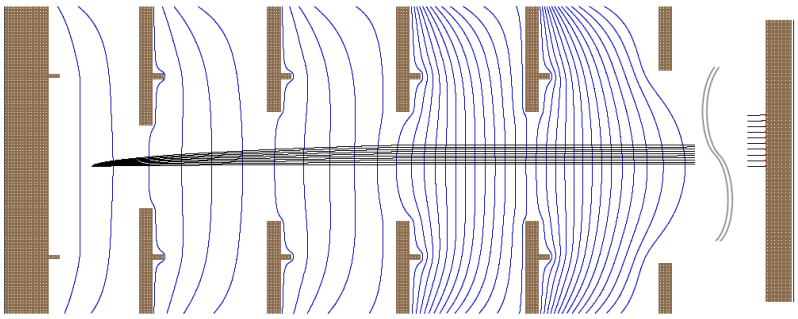

(c) Simulated flight path of differnt starting velocities.

Figure 3.12: SIMION simulations obtain a magnification factor M = 0.72 for velocities in the x- and y-direction and M_t = -35.6·10^{-3} s^2 m^{-1} for the z-direction. All simulations are done with the 2-kV setting with m = 29 amu.

3.2.5 The data acquisition

For each detected event, the differential cross section $\frac{d^3\sigma}{dv_x dv_y dv_z}$ is measured by determining the three dimensional velocity (v_x, v_y, v_z) of the scattering product. To generate the scattering images for one energy, about 30 000 events are collected. Depending on the cross section and the production rate of the ions this takes about 10 hours up to more than one day of acquisition time. Isolating the target mass of other fragments is done by setting the correct time window on the MCP. To evaluate the data, the position and the time information is converted into the product velocity vector and then transformed into the centre of mass frame. This transformation involves substituting the velocities of collision partners by their equivalent velocities in the centre of mass frame by calculating first the centre of mass (c.m.) velocity

$$v_{c.m.} = \frac{\sum_i m_i v_i}{\sum_i m_i} \,. \tag{3.14}$$

Taking this into account, the kinetic energy of the system can be split up into the kinetic energy of the centre of mass and the relative kinetic energy of the two collision partners

$$E_{kin} = \frac{1}{2} m_1 v_1^2 + \frac{1}{2} m_2 v_2^2 = \frac{1}{2} M v_{c.m.}^2 + \frac{1}{2} \mu v^2 \tag{3.15}$$

$$\text{with} \quad M = m_1 + m_2, \quad \mu = \frac{m_1 m_2}{m_1 + m_2}, \quad v = v_1 - v_2$$

being M the sum of the implied masses, μ the reduced mass of the system and v the relative velocity of both particles, which is a direct measurement of the available translational energy [66]. Therefore a single particle starting from the scattering centre $r = 0$ can be assumed. This particle with the reduced mass m is moving with an initial translational energy and angular momentum, which are conserved respectively. Fig. 3.13 shows a Newton diagram, where the relation between the velocities in the centre of mass frame and in the laboratory frame are expressed. This diagram illustrates the equation (3.14) in its equivalent form:

$$v_1 = V + \frac{m_2}{M} v \qquad v_2 = V - \frac{m_1}{M} v. \tag{3.16}$$

The Newton diagram in Fig. 3.13 shows an example of a scattering event with two particles. The solid arrows (red and blue) denote the velocities of the neu-

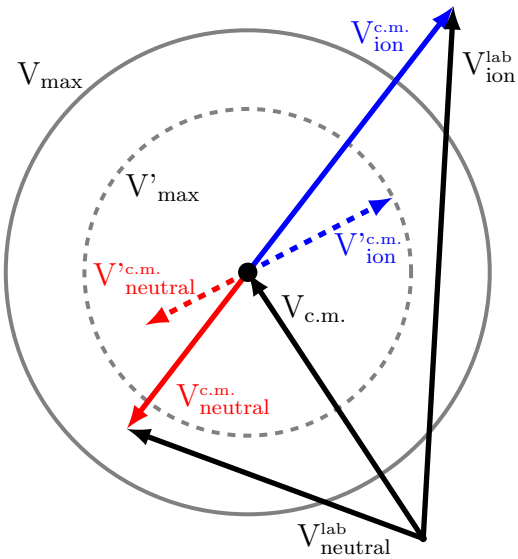

Figure 3.13: Newton diagram for a scattering event with two particles. The scattering process is cylindrically symmetric with respect to the relative velocity axis. The outer circle marks the kinematic cut-off, given by the maximum product velocity that can occur taking into account that the energy and momentum is conserved. The dashed inner circle marks the kinetic energy, due to transformation from kinetic energy to internal excitation.

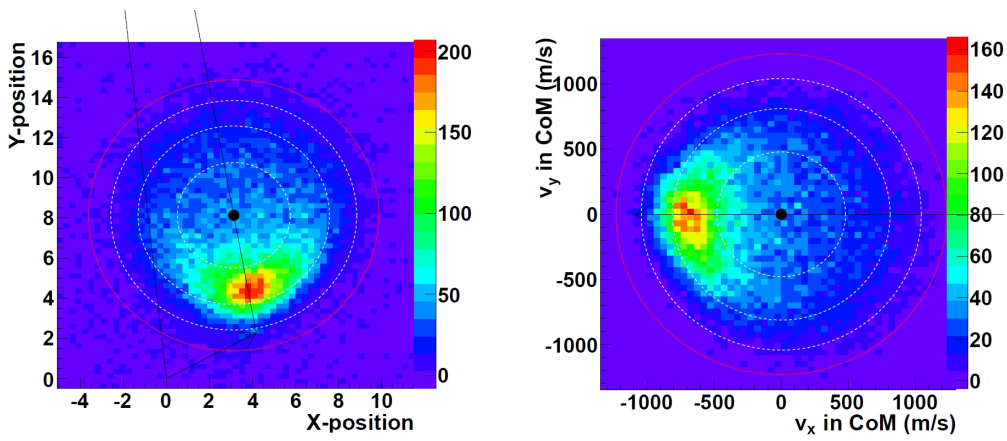

(a) Raw picture of scattering events on the detector displayed by the CCD-camera.

(b) Transformed picture into the centre-of-mass frame and rotated horizontally to the scattering axis.

Figure 3.14: By using equation (3.12) the position on the detector is transformed into the velocities respectively. The red circle represent the kinematic cut-off, whereas each dashed white circle illustrates a kinematic energy loss of 1 eV.

tral molecule and the ion respectively. After the collision process, the maximum energy of the ion is depicted by the outer solid circle which represents the kinematic cut-off. This circle corresponds to a collision where the kinetic energy is conserved and no kinetic energy is transformed into internal energy [66]. The dashed inner circle depicts exemplarily a collision where some of the initially available kinetic energy is transferred into internal excitations of the products. As a consequence of the kinetic energy loss one can directly measure the sum of the internal degrees of freedom of the products. The momentum of each collision has to be conserved.

In addition, the distribution in the centre of mass frame is rotated such that the relative velocity vectors align horizontally along the collision axis v_x. A comparison of the raw image on the detector and the rotated distribution in the centre of mass frame is shown in Fig. 3.14.

3.3 Description of imaging uncertainties

After the detection of the product ion on the detector, one has to take into account that there are different sources of uncertainties for the ion energy, ranging from imaging errors of the VMI spectrometer, caused by the offset and uncertainty of the starting position of the ion to the finite resolution of the ion beam and neutral beam.

3.3.1 Uncertainty of the VMI spectrometer

As already described in section 3.2.2 the first order matrix for the velocity map imaging shows not only a value in $\frac{\partial R}{\partial v_r}$ but also a small value of $\frac{\partial R}{\partial r}$. This means that the position of the detected ion on the detector depends not only on the starting velocity, but also on the starting position. Due to the fact that the velocity of the product ion is calculated from the position on the detector, the determined velocity depends also on the starting position and not only on the velocity in the scattering regime. This blurring effect on the product ion velocity and is determined by taking a SMI image of the product ions as shown in Fig. 3.15. An offset of the starting position of 1.3 mm in x-direction and 1.4 mm in y-direction (with respect to the zero-point) is obtained from this image and a width of 2.5 mm can be assumed.

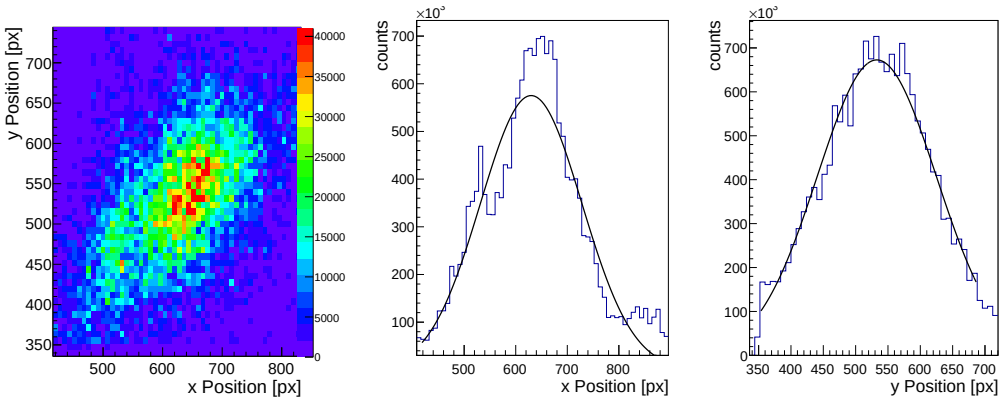

(a) SMI of the product ions.

(b) Spatial distribution in the x-axis; $\Delta y = 1.3\,\mathrm{mm}$

(c) Spatial distribution in the y-axis; $\Delta y = 1.4\,\mathrm{mm}$

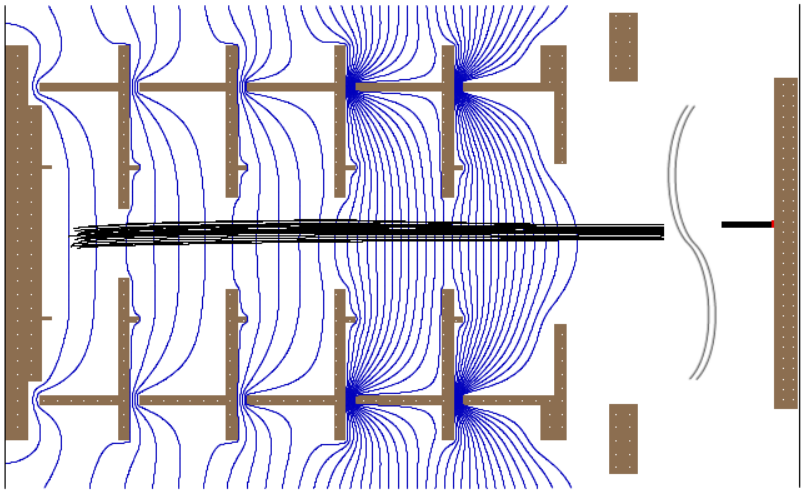

(d) SIMION simulations with the determined offset and width of the starting point in the scattering region. This leads to a blurring on the detector which corresponds to 36 m/s (for a relative energy of 1.85 eV).

Figure 3.15: SMI picture of the products to determine the offset and the width of the starting position of the produced HCO^+ and HOC^+ ions. With this information the influence of the starting position on the velocity uncertainty can be simulated with SIMION.

To know the influence of the starting position the matrices for the 2-kV setting of the VMI spectrometer could be calculated. Another method is to do simulations in SIMION for the given potential of the spectrometer and the starting position (Fig. 3.15(d)). By simulating the position on the detector with multiple starting points, which are Gaussian distributed around the measured offset, the velocity spread due to the given starting point can be determined. These simulations are then performed for all different relative kinetic energies (see Tab 3.1).

Table 3.1: Velocity blurring of the product ion due to the uncertainty of the starting point. The starting point is Gaussian distributed with $\sigma = 1.1\,\mathrm{mm}$.

collision energy [eV]	mean velocity [m/s]	velocity uncertainty [m/s]
0.20	360	39
0.65	485	34
1.85	775	36
2.50	920	43
4.40	1 140	51

3.3.2 Ion and neutral beam uncertainties

In addition to the uncertainty due to the VMI spectrometer as described in the previous section there is an uncertainty caused by the given quality of the ion an neutral beam. The velocity spread of the neutral CO beam is constant over all measurements and is given by a sigma of 165 m/s. For the ion beam the energy spread depends on the used energy. The resulting velocity spread of the produced ion after the collision is calculated by taking the uncertainties of the ion beam velocity and angle, the molecular beam velocity and angle and the given masses before and after the collision as described in [32]. An example for specific conditions is shown in Fig. 3.16. In this plot, which represents the velocity resolution in the centre of mass frame, one can see two different rings. The outer one is for the kinematic cut-off as described in section 3.2.5 where the inner ring is the velocity resolution at a given energy loss caused by the inner excitation of the molecules after the scattering reaction, namely 40% internal excitation fraction.

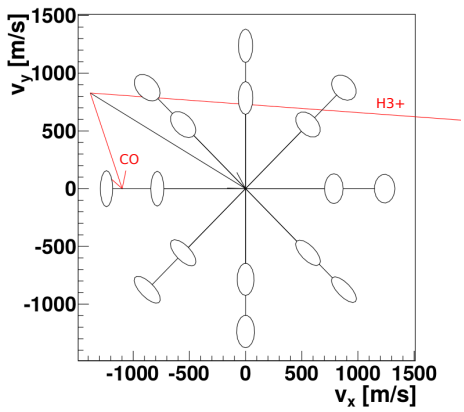

Figure 3.16: Estimation of the velocity resolution due to the velocity spread of the ion and neutral beam, calculated by Gaussian error propagation (see [32]). The two rings show the kinematic cut-off and a resulting velocity for a given internal excitation of the product ion.

3.3.3 Error budget and systemetics

After determining the velocity resolution due to the imaging uncertainty of the spectrometer and the finite velocity spread of the reactant beams these two errors have to be merged. As there is no correlation between these two errors Gaussian error propagation for uncorrelated errors is applied

$$\sigma_f^2 = \sum_i^n \sigma_i^2 \,. \tag{3.17}$$

This leads to a pre existing velocity resolution σ_{pre} which is independent of any internal excitation of the products and just depends on the velocity spread due to technical issues σ_{tech} and the velocity uncertainty σ_{VMI} given by the imaging properties of the VMI spectrometer

$$\sigma_{pre} = \sqrt{\sigma_{tech}^2 + \sigma_{VMI}^2} \tag{3.18}$$

In section 4.2.5 this error propagation will be used and described in more detail in order to discuss the broadening of the internal energy (E_{int}).

Chapter 4

Results and discussion

In this section the results of the investigated reactions producing the formyl isomers HCO^+ and HOC^+ are presented. First the reaction H_3^++CO is discussed and in a later section the results of the reaction $HOCO^+$+CO are shown. To analyse the ion-molecule reaction the energy or rather the velocity distribution of the ion and neutral beam are shown, together with their resolution. Afterwards the scattering images are presented together with a discussion of the internal energy distribution and their angular dependence. Due to the different time of flight for unequal masses, isotopes of carbon can be detected as well as carbon monoxide cations. The ratio of these masses are compared for the different relative energies of the reactants. As a result of the different binding energies of the HCO^+ and HOC^+ isomers the kinetic energy and therefore the velocity of the ions after the collision process depends on the enthalpy respectively. Thus, these two isomers should be on different circles on the Newton diagram. Due to energy broadening the two isomers cannot be separated directly. Section 4.2.5 describes a model to fit the measured internal energy distribution, which explains how an upper bound for the ratio of HOC^+ can be estimated. Before showing the results of the measurements a motivation for the two different reactions (H_3^++CO and $HOCO^+$+CO) is shown.

4.1 Newton diagrams of the two reactions

As already discussed the reaction H_3^++CO→HCO^+/HOC^++H_2 is a key reaction to understand the chemical composition in the interstellar medium. Another reaction contributing to the formation of HCO^+ and HOC^+ is the reaction involves

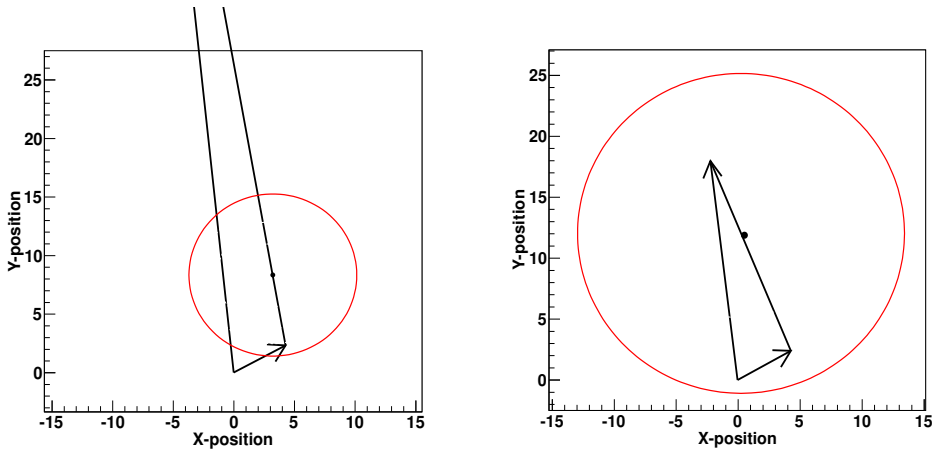

(a) H_3^++CO → HCO^++CO with a relative energy of 1.85 eV.

(b) $HOCO^+$+CO → HCO^++CO_2 with a relative energy of 0.8 eV.

Figure 4.1: Newton diagrams for the two reactions. The arrow which points up is the H_3^+ and $HOCO^+$ respectively. The arrow from the left to the right side depicts the CO beam where the red circle is the kinematic cut-off for the HCO^+ cation. Units of the diagrams in mm.

the cation $HOCO^+$. The two reactions are quite different in their dynamics because the mass ratios of the two educts (H_3^+/CO and $HOCO^+$/CO) is different. This difference in the mass ratio leads to totally different Newton diagrams (see Fig. 4.1). As one can see, the velocity vector of the H_3^+ beam compared to the CO beam is enormous.

4.2 H_3^+ + CO

The most important reaction to form HCO^+ in the interstellar medium is the reaction

$$H_3^+ + CO \rightarrow HCO^+ + H_2 \qquad (\Delta H = -1.76\text{eV}) \tag{4.1}$$

which also forms the isomer HOC^+ by the reaction

$$H_3^+ + CO \rightarrow HOC^+ + H_2 \qquad (\Delta H = -0.13\text{eV})\,, \tag{4.2}$$

where ΔH is the enthalpy of the reaction. This reaction is studied experimentally at five different relative energies to preserve energy dependent scattering results. The energies are 0.20 eV, 0.65 eV, 1.85 eV, 2.50 eV and 4.40 eV. As de-

scribed in section 3.1.1 the H_3^+ are produced by plasma discharge and focused into the scattering chamber after they are stored and cooled in an ion trap. By setting the offset potential of the VMI spectrometer to a given voltage the ions are decelerated to the required energies. Using the VMI settings of the imaging spectrometer the kinetic energy of the ions can be measured. Changing the settings of the ion trap, i.e. radio frequency, trapping time and endcap voltage, increases the energy resolution of the ion beam. Fig. 3.6 shows such a measurement for the ion beam with 2.05 eV. Tab. 4.1 shows the H_3^+ energies and the corresponding standard deviations of the internal energy. The variation of the mean energy and the standard deviation are caused by multiple measuring cycles of the same energy. During these cycles the energy of the ion beam is drifting. After a scattering time of about two hours the energy of the ion beam is controlled to make sure that the drift is not to high and if necessary the beam is aligned again.

Table 4.1: Table of the H_3^+ ion energies used in the experiment. The mean values and the sigmas are shown as well as the relative energies of the two reactant beams.

energy [meV]	σ [meV]	E_{rel} [eV]
280	122	0.20
700	133	0.65
2 120	190	1.85
3 010	340	2.50
5 060	243	4.40

4.2.1 Time of flight spectrum of CO^+, HCO^+ and $H^{13}CO^+$

After the crossing of the reactant beams the plates of the VMI spectrometer are switched to their working potential and the produced ions are accelerated towards the detector. The MCP of the detector is active in the time interval of 6 μs - 8 μs, due to the fact that the time of flight for the HCO^+ ions is simulated with SIMION to be 7.2 μs for the 2 kV settings. During this time all ions with an according mass are detected. Fig. 4.2(a) shows a typical time of flight spectrum where the time axis starts at the time at which the MCP is active.

Three different ion species are observed. To identify the two small peaks better the major one is scaled down by the factor 30. The main peak at $\sim$7500 ns is the signal of the HCO^+ and HOC^+ ions with mass m = 29 amu where the minor

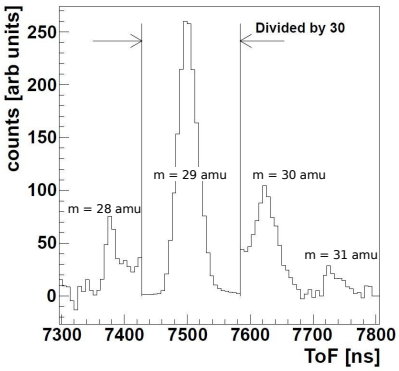

(a) Time of flight spectrum for the detected ions. The peak of m = 29 amu is scaled down by 30 to see the small peaks better.

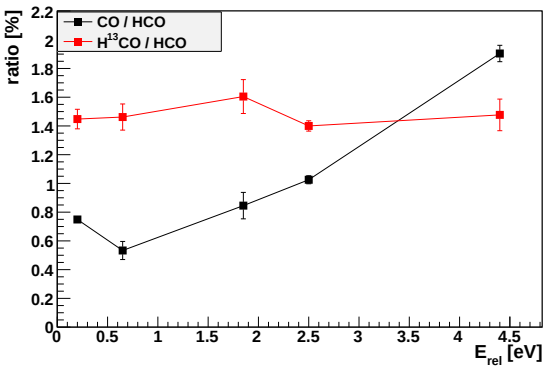

(b) Ratios in % of the detected peaks for all measured relative energies. The ratio of $H^{13}CO^+$ is constant for all energies where the CO^+ peak is more present at the relative energy of 4.4 eV. The error bars result from the varied cuts (± 5 ns) for each mass.

Figure 4.2: Time of flight (TOF) of the produced ions where the masses m = 28 amu, m = 29 amu and m = 30 amu show a clear peak. Also mass m = 31 amu appears in a tiny peak. These masses belong to CO^+, HCO^+, $H^{13}CO^+$ and $HC^{18}O^+$.

peak at ∼ 7380 ns corresponds to the mass m = 28 amu. This peak is supposed to be CO^+. The third peak at ∼ 7625 ns accords to the mass m = 30 amu and is most likely given by the carbon isotope ^{13}C. So the peak corresponds to $H^{13}CO^+$ and $HO^{13}C^+$. Also a little contribution of DCO^+ would be found in this peak, but this is negligible, as the natural isotopic abundance of deuterium is only 0.0156% [67].

By setting a cut[1] with slightly varied edges (± 5 ns) the number of counts for all ions of the three peaks is determined. This is done for all five relative kinetic energies and the ratios CO^+/HCO^+ and $H^{13}CO^+/HCO^+$ respectively are depicted in Fig. 4.2(b). The error bars appear due to the variation of the time cuts for the three peaks.

The proportion of $H^{13}CO^+/HCO^+$ is for all energies almost constant at 1.45%. The NIST database [67] declare this proportion to be 1.09%. The higher value in the measurements is caused by the width of the HCO^+ peak, so that some hits of this peak are wrongly counted as mass m = 30 amu. In Fig. 4.2(a) one can also see a tiny peak at a time of flight of ∼ 7725 ns. This peak belongs

[1] only taking the counts into account which are in a defined time interval between two edges

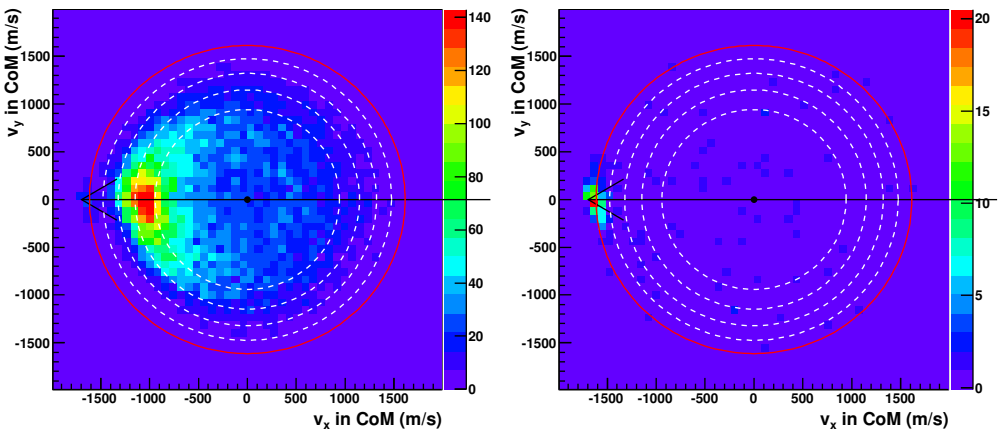

Figure 4.3: Scattering image for 4.40 eV relative energy. In the left picture the time of flight window is set for CO^+, HCO^+ and $H^{13}CO^+$ (m = 28, 29 and 30 amu). At the end of the CO arrow in the Newton diagram a blob is present. By setting the time of flight only for the CO^+ ions one can see in the right picture that the blob is generated by these ions.

to m = 31 amu and is for all energies about 0.2% of the HCO^+ peak. The isotopic percentage of the ^{18}O isotope is about 0.2% [67]. Thus, this peak has to be $HC^{18}O^+$. By looking at the scattering image of the $H^{13}CO^+$ and $HC^{18}O^+$ ions one can see that these show the same dynamic features as the HCO^+ ions. This is caused by the same chemical characteristics because only the nucleus is different in both cases.

By looking at the behaviour of the proportion of CO^+/HCO^+ in Fig. 4.2(b) one can see a rise for higher collision energies, especially for the energy of 4.4 eV. Due to the fact that for all energies the CO^+ peak is existing, the possibility of creating this cation in the molecular CO beam is considered. If this is the case, the CO^+ counts are correlating with the measuring time for each energy because the molecular CO flux is constant for the whole experiment. One can observe a positive correlation between loop numbers (duration of the measurement) and CO^+ events. This would be a indication for CO^+ that is produced in the molecular beam source. However, as the appearance energy to form $CO \rightarrow CO^+$ is 19.5 ± 0.2 eV [68] it is unlikely that this really happens.

By anticipating the results of the TOF spectrum of the $HOCO^+$+CO experiment (compare section 4.3.2), where no peak for the CO^+ cation appears, one can exclude the possibility that these ions are created in the neutral beam

source. Because if the CO^+ ions would be produced in the neutral beam source, there must be also a peak in the $HOCO^+$ experiment.

For the $H^{13}CO^+$ and $HC^{18}O^+$ ions the scattering images are the same than for the HCO^+ ions. This is not the case for the CO^+ ions (see Fig 4.3). There the ions appear just at the position of the neutral CO beam. This implies that the ions are either directly formed in the molecular CO beam or that a dissociative charge transfer from the H_3^+ takes place: $H_3^+ + CO \rightarrow H_2 + H + CO^+$.

4.2.2 3D-Velocity Images

After the collision of the reactant beams the product ions are imaged onto the detector as described in section 3.2. This signal is then converted into a velocity. The velocity $v_{x,y}$ parallel to the extraction plates corresponds to the position R on the detector and the velocity v_z in direction of the spectrometer axis depends on the difference in the flight times. For some reason v_z cannot be calculated as described in equation 3.13. This was also tried by [52, 54] but no real cause was found. Assuming that the velocity distribution of the products after the collision process is cylindrical symmetric the width of the v_y and v_z distribution has to be identical [1]. By taking the known distribution of v_y, one can transform the information from the time of flight into v_z. By knowing the components in y- and z-direction the radial velocity is calculated by

$$v_r = \sqrt{v_y^2 + v_z^2}\,.$$

In Fig. 4.4 the 3D scattering images for the five collision energies are presented with the corresponding Newton diagrams. The red circles depict the kinematic cut-off and the dashed white circles represent kinetic energies reduced by 1 eV respectively. At a glance one can see that for all energies the velocities are clearly lower than the kinematic cut-off. Furthermore forward scattering in direction of the CO molecule appears as the mayor mechanism. For increasing relative collision energies the energy loss increases as well.

[1] The picture is already transformed into the centre of mass frame and rotated horizontally to the scattering axis - compare with Fig. 3.14(b).

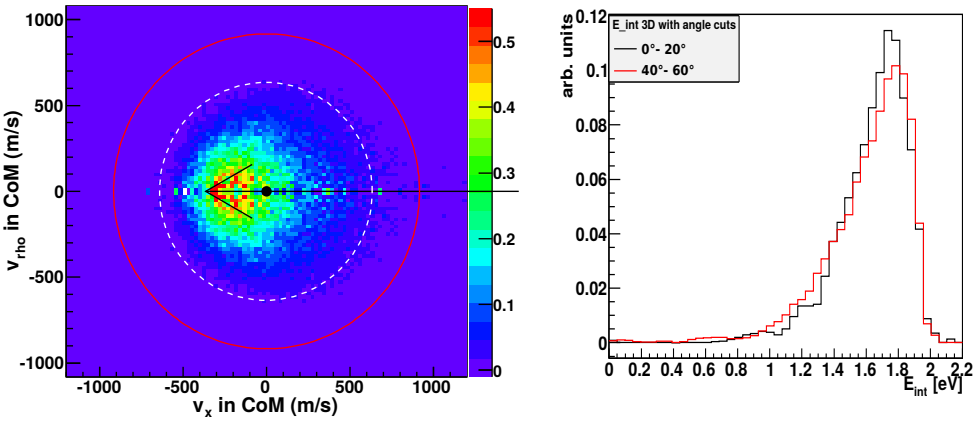

(a) **0.20 eV**

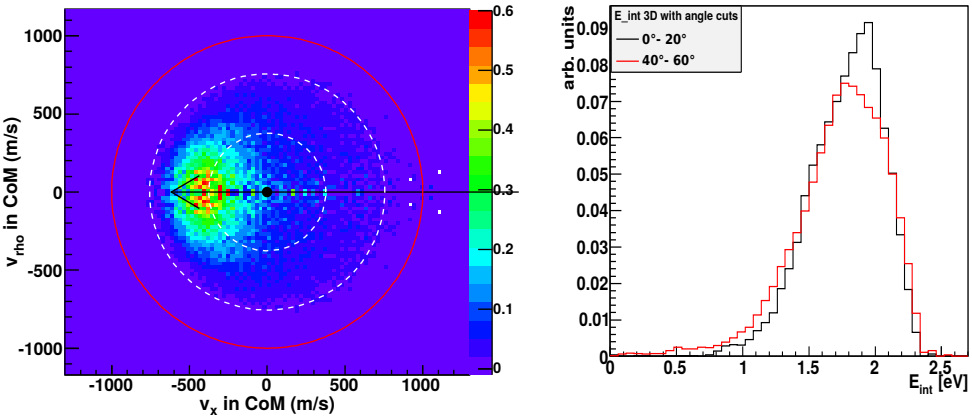

(b) **0.65 eV**

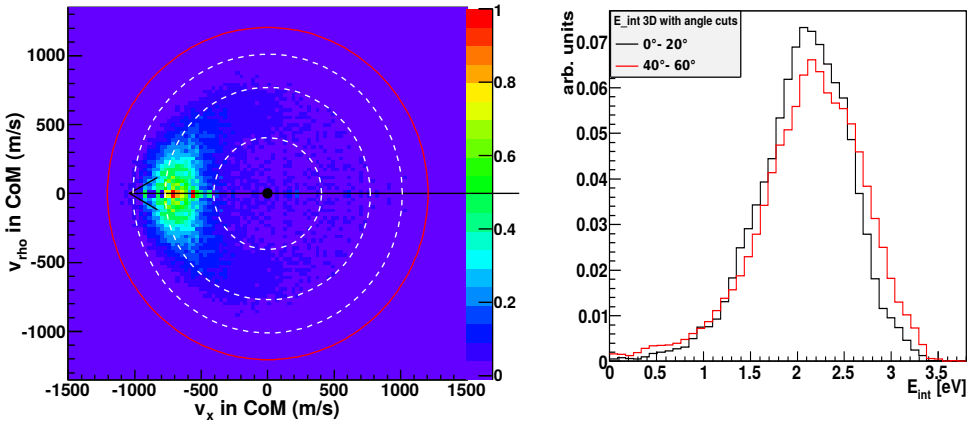

(c) **1.85 eV**

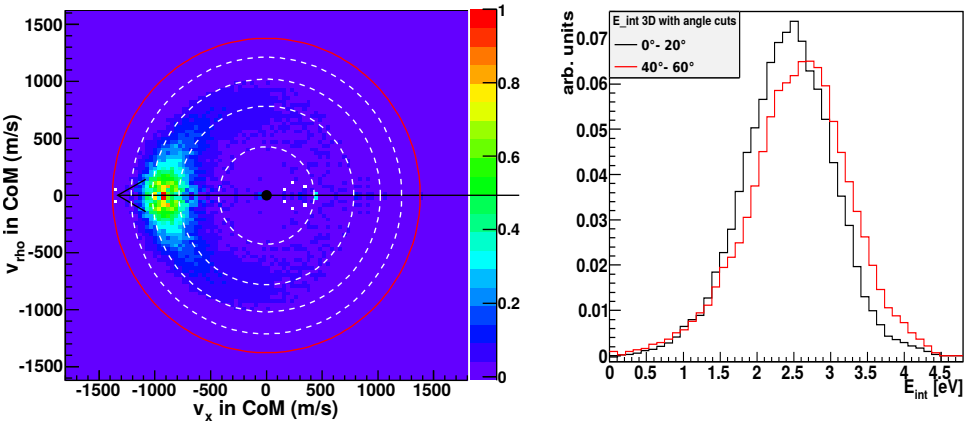

(d) **2.50 eV**

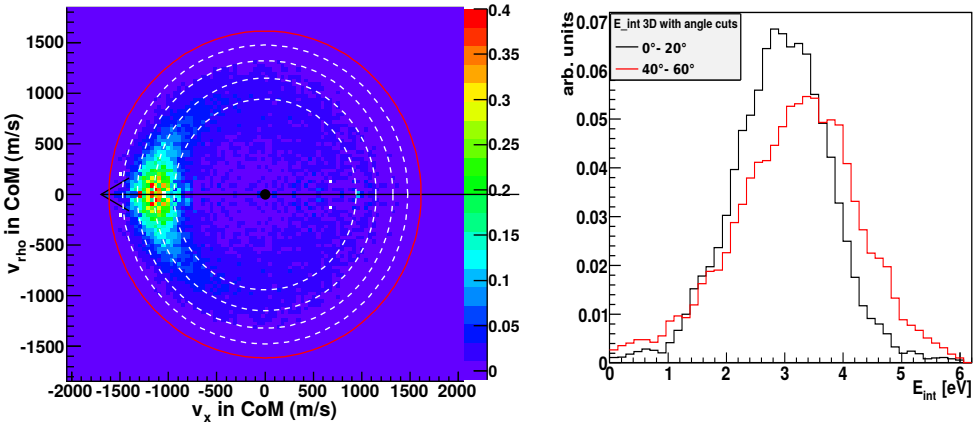

(e) **4.40 eV**

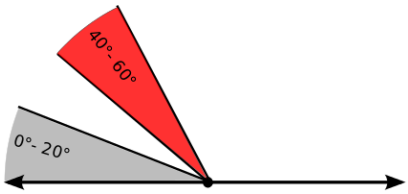

(f) Definition of the scattering angels.

Figure 4.4: 3D-velocity images and internal energy distributions. In the left plots the 3D scattering images for all experiments are shown. The black arrows correspond to the velocities of the reactant beams and the circles represent the Newton diagram as described in the text.
In the right graph the internal energy distribution for two different scattering angle areas are plotted, where the black line represent forward scattering ($10° \pm 10°$) and the red one shows the internal energy for ions with a scattering angle of $50°(\pm 10°)$.

4.2.3 Angular dependence

The right graphs in Fig. 4.4 show the angular dependence of the internal energy where the histograms are normalized to allow a comparison of the distributions. For the low collision energies, like 0.20 eV and 0.65 eV, no shift in the internal energy is observed at higher energies a shift to more internal energy and also a broader energy distribution is identified. The higher internal energies for larger scattering angles are related to the impact parameter. Due to the fact that a smaller impact parameter leads to a higher scattering angle, one can say that a collision with small impact parameter has to produce more internal excitations.

Recently Trippel and coworkers have investigated the angular differential state-to-state cross sections as a function of the collision energy in the reaction $Ar^+ + N_2 \rightarrow Ar + N_2^+$ [69]. They obtained a dominant excitation for the $\nu' = 1$ vibrational level of the molecular nitrogen cation. Higher vibrational excitations up to $\nu' = 6$ have been observed for large scattering angles. Their results of the vibrational level-dependence of the angular cross section agree with the model presented by Candori and coworkers who obtained the vibrational levels of N_2^+ from curve crossing probabilities for vibrationally-adiabatic intermolecular potentials [70]. Their model shows, that for a particular product vibrational state ν', the yield changes strongly with the impact parameter and is thus correlated to the scattering angle.

This explains, why larger scattering angles result in more internal energy and the internal energy is broader .

4.2.4 Internal excitation of the products

The internal energy of the products after the collision is determined by taking the difference of the kinetic energies of the reactants and the products after subtracting the enthalpy. As one can see in Fig. 4.4 the internal energy of all different relative energies is considerably high. The energy has not only redistributed into the HCO^+ system but also in the second collision product, H_2. One can say that both products are internal excited after the collision takes place. Due to the existence of multiple vibrational modes in HCO^+/HOC^+ and H_2, it is not possible to quantify the exact vibrational distribution from the obtained internal energy distribution

The NIST database provides values for the stretching and bending modes

of the HCO^+ formyl cation [71]. In the results of Stamatiadis and Werner the stretching and bending modes of the neutral HCO molecule are shown [72, 73]. There one can see that the existence of two excitation modes at the same time leads nearly to a superposition of the energies of the two separate excitation modes. Doing this with the results of the HCO^+ values of the single excitation modes gives an approximation for the energies with more than one excited mode. The variation of the values for the frequencies in Tab. 4.2 results from the difference in the values given by NIST [71].

Table 4.2: Vibration and bending modes of the HCO molecule: ν_1 is the H-C strech mode, ν_2 the C-O strech mode and ν_3 is the bending mode. Frequency and energy with respect to the $\nu_{1,2,3} = 0$ level [74].

Mode (ν_1,ν_2,ν_3)	Freq. (cm^{-1})	Energy (eV)
(1,0,0)	2 973±134	0.368
(0,1,0)	2 159±34	0.268
(0,0,1)	829	0.102
(1,1,0)	5 132	0.636
(1,0,1)	3 802	0.471
(0,1,1)	2 988	0.370
(1,1,1)	5 961	0.739

For the H_2 molecule the vibrational zero point energy is 2 200.6 cm^{-1} [75]. As the energy levels of a harmonic oscillator

$$E(\nu) = \left(\nu + \frac{1}{2}\right)\hbar\omega \tag{4.3}$$

are equally spaced by $\Delta E = \hbar\omega$ the energies for the vibrational quantum numbers $\nu = 0, 1, 2, \ldots$ can be calculated (see Tab. 4.3). The plots of the internal energy (Fig. 4.4) show a maximum at 1.7 eV, 1.9 eV, 2.1 eV, 2.4 eV and 3.0 eV for the five different energies. As these internal energies are appearing as excitations in the vibration modes of the product molecules, one can say that more than one mode is excited. In Tab. 4.2 also the superposition of the first excited modes and their corresponding energies are shown. These energies are not large enough to cover the whole internal energy. Thus, more than the first modes have to be excited. Due to the large amount of possible excitation combinations of the different vibration modes of HCO^+ and H_2, a precise determination cannot be carried out.

Table 4.3: Vibration energies of the H_2 molecule, where ν is the vibrational quantum number [60, 75].

ν	Freq (cm^{-1})	Energy (eV)
0	2 200	0.273
1	6 601	0.818
2	11 003	1.364
3	15 404	1.910
4	19 805	2.455

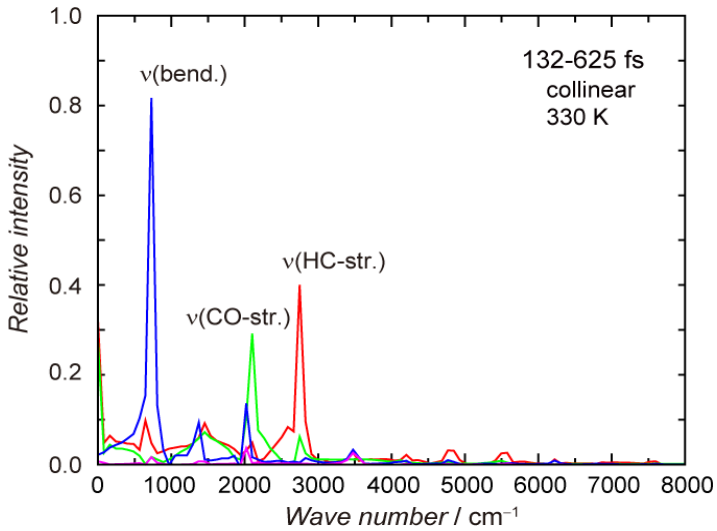

Figure 4.5: Different excitation modes in the $H_3^+ \cdots CO$ complex. Intramolecular vibrational energy redistribution calculated by Hirano and coworkers for a collinear approach of the H_3^+ to the C end of CO at 330 K (taken from [44]).

In 2009 Hirano and coworkers were studying the linear approach from H_3^+ to the C end of CO with translational temperatures of 20 K (a typical kinetic temperature of dark clouds) and 330 K (a typical translational temperature for ions in a glow discharge) in direct dynamics calculations [44]. In the first 100 fs of the approach the H^+ is attracted to the CO and forms HCO^+, where the H–C stretching mode is highly excited. This excitation can then relax within the same vibrational ladder or be transferred into the bending mode. The relative intensities of the different excitation of the HCO^+ is shown in Fig. 4.5. Although excitations of higher vibrational levels are seen, the majority of the products are populated in the fundamental vibrational states. This may change at higher collision energies, as we are using in our experiments.

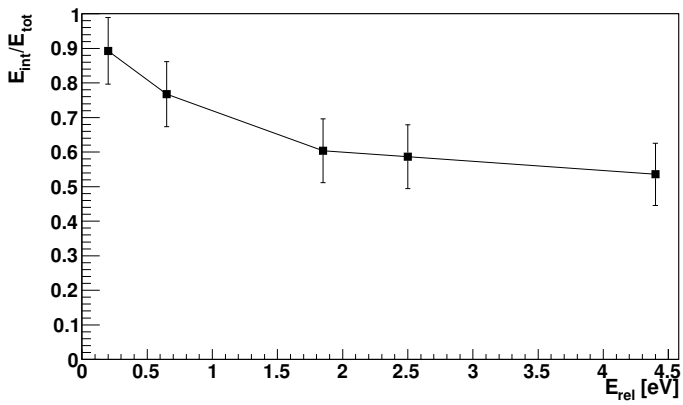

Figure 4.6: Ratio of the internal energy and the total energy as a function of the relative energy. The total energy is the sum of the relative energy and the exothermicity. The error bars depict the RMS of the internal energy.

As discussed in section 4.2.3, Candori and coworkers showed for the reaction $Ar^+ + N_2 \rightarrow Ar + N_2^+$ that the excitation of the ν' level for N_2^+ depends on curve crossing probabilities for vibrationally-adiabatic intermolecular potentials [70]. In our reaction we have not only one possible vibrational state but three, one in the H_2 molecule and two in the HCO^+ cation, which has also an additional bending mode. Thus, much more curve crossings are possible, which lead to the excitation of one or more of these vibrational modes.

Fig. 4.6 shows the ratio of maximum internal energy E_{int} (taken from Fig. 4.4) to total available energy E_{tot} as a function of the relative energy E_{rel} of the two reactant beams. The total energy is the sum of the relative energy and the enthalpy. One can see that for higher relative energies the ratio decreases and it reaches a value of ~ 0.5 for the highest entry.

By now, only the vibrational modes of the products are considered. The rotational constants for HCO^+ and H_2 are 0.185 meV and 7.53 meV respectively [40, 76, 75]. Regarding the rotational energy levels of the molecules, which can be described using the rigid rotor model, the energies are

$$E_J = B_0 J\,(J+1)\,, \tag{4.4}$$

where J is the rotational quantum number $(0, 1, 2, 3, ...)$ and B_0 is the rotational constant. For the H_2 molecule a rotational energy of nearly 1 eV is reached for $J = 11$. Due to the low rational constant for the HCO^+ cation, the model of

the rigid rotor is no good approximation. Nevertheless, the rotational energy of the HCO^+ must be taken into account, if one is looking for possible populated internal excitations of the products.

In total there are several possibilities in which the kinetic energy can be transformed. One can not really say, in which type of energy it is converted but most likely all of them are excited at least in the first mode, especially for higher relative energies where also the internal energy is higher.

4.2.5 Ratio of HOC^+ / HCO^+

The main task of this work is to determine the ratio of the formyl isomer HOC^+ depending on the relative kinetic energy of the two reactant beams. Due to the lower proton affinity of the oxygen in the carbon monoxide the enthalpy of the reaction $H_3^+ + CO \rightarrow HOC^+ + H_2$ is lower than in the reaction where HCO^+ is formed. Thus, the kinematic cut-off of the observed HOC^+ ion appears 1.63 eV lower. By looking at the plots of the internal energy (Fig. 4.4) one should see two separated peaks, one for the HCO^+ and one for the HOC^+ channel respectively. As already discussed in section 4.2.4 the internal excitations of the products are quite high.

By assuming that the internal excitation does only depend a little on the formed isomer, one can say that the percentage energy loss due to internal excitations compared to the maximum available energy for both isomers has to be the same. With this assumption one can calculate the position of the mean value of the HOC^+ isomer if the position of the HCO^+ peak is known. Due to the high internal excitation of the products, the distance between the two peaks of the HCO^+ and HOC^+ isomer is reduced. Together with the broadening of the peak due to the distribution of the internal energy, it is not possible to see two different peaks. For lower collision energies this effect is even more critical, as the percentage of the internal energy compared to the maximum available energy is higher and so the distance of the two peaks will decrease even more.

To find a fit function, which describes the measured internal energy as a superposition of the internal energy of both two isomers a second assumption has to be made. It is assumed that the velocity of the cations after the collision process are Gaussian distributed[1]. With these two assumptions a fit function for

[1]This distribution is chosen, because this distribution leads to a very good fit for the case of forward scattering.

the internal energy distribution can be constructed.

$$p(\vec{v}_{HCO}) = A \cdot \exp\left(-\frac{(\vec{v}_{HCO} - \vec{v}_0)^2}{2\sigma^2}\right) \tag{4.5}$$

where A is a factor to normalize the Gaussian function and $\vec{v}_0$ is the velocity of the mean value of the energy distribution. The relation between the density function of the velocity and the density function of the internal energy is given by

$$p(v)dv = -p(E_{int})dE_{int} \quad \rightarrow \quad p(E_{int}) = -p(v)\frac{dv}{dE_{int}}\,. \tag{4.6}$$

When the measured velocity of the ion increases the internal energy decreases. This is the reason for the minus sign.

$$E_{int} = E_{kin} - E'_{kin} - \Delta H \tag{4.7}$$

where E'_{kin} is the relative energy after, E_{kin} the relative energy before the collision and ΔH is the enthalpy of the reaction (for HCO^+ ΔH = -1.76 eV and for HOC^+ ΔH = -0.13 eV).

$$E'_{kin} = \frac{1}{2}\mu' \cdot \vec{v}'^{\,2} \tag{4.8}$$

with the reduced mass μ' of the HCO and H_2 molecule and the relative velocity $\vec{v}'$. In the centre of mass the momentum is zero, so the momenta of the two molecules are the same

$$\vec{p}_{HCO} = -\vec{p}_{H_2} \quad \rightarrow \quad \vec{v}_{H_2} = -\frac{m_{HCO}}{m_{H_2}}\,\vec{v}_{HCO}\,. \tag{4.9}$$

In this model only forward scattering is taken into account, as the main part of the scattered ions are forward scattered, so $\vec{v}$ becomes v.
With $v' = v_{HCO} + v_{H_2}$, because the velocities are in the centre of mass frame in the opposite direction, the relative kinetic energy after the collision process is

$$E'_{kin} = \frac{1}{2}\mu'\left(\frac{m_{H_2} + m_{HCO}}{m_{H_2}}\right)\vec{v}^{\,2}_{HCO} = a \cdot \vec{v}^{\,2}_{HCO} \tag{4.10}$$

and the internal energy is

$$E_{int} = E_{kin} - a \cdot v^2_{HCO} - \Delta H \tag{4.11}$$

where a is the prefactor of E'_{kin} described by the masses.

$$v_{HCO} = \sqrt{\frac{E_{kin} - \Delta H - E_{int}}{a}} \quad , \quad v_0 = \sqrt{\frac{E_{kin} - \Delta H - E_{0_{HCO}}}{a}} \tag{4.12}$$

By assuming that the enthalpy ΔH is independent of the internal energy E_{int}

$$\frac{dv_{HCO}}{dE_{int}} = -\frac{1}{2a} \cdot \frac{1}{\sqrt{\frac{E_{kin}-E_{int}-\Delta H}{a}}} \,. \tag{4.13}$$

With $\frac{dv}{dE}$ and the expression for v and v_0 one gets

$$p(E_{int_{HCO}}) = \frac{A \cdot exp\left(-\frac{\left(\sqrt{E_{kin}-\Delta H_{HCO}-E_{int}}-\sqrt{E_{kin}-\Delta H_{HCO}-E_{0_{HCO}}}\right)^2}{2\sigma^2\, a}\right)}{2a\sqrt{\frac{E_{kin}-\Delta H_{HCO}-E_{int}}{a}}} \tag{4.14}$$

This is the function for the internal energy distribution of HCO^+ if one assumes that the velocity is Gaussian distributed. In this function the parameters A, E_0 (the mean value of the energy distribution) and σ are free parameters and they could be used for fitting the function to the internal energy distribution if one only takes the HCO^+ isomer into account. By taking the assumption that the relative energy loss (in %) is equal for both isomers, one obtains

$$\frac{E_{0_{HOC}}}{E_{kin} - \Delta H_{HOC}} = \frac{E_{0_{HCO}}}{E_{kin} - \Delta H_{HCO}} \tag{4.15}$$

and that the σ is the same for both energies the fit for the second isomer is

$$p(E_{int_{HOC}}) = \frac{B \cdot exp\left(\frac{-\left(\sqrt{E_{kin}-\Delta H_{HOC}-E_{int}}-\sqrt{E_{kin}-\Delta H_{HOC}-E_{0_{HOC}}}\right)^2}{2\sigma^2\, a}\right)}{2a\sqrt{\frac{E_{kin}-\Delta H_{HOC}-E_{int}}{a}}} \tag{4.16}$$

where the factor A is replaced by the factor B. The superposition of both probability density functions produces the fit function for both isomers

$$p(E_{int}) = p(E_{int_{HCO}}) + p(E_{int_{HOC}}) \,. \tag{4.17}$$

In section 3.3.3 the uncertainty of the educt beams σ_{tech} and of the VMI spectrometer σ_{VMI} are discussed. To account for the whole width of the measured

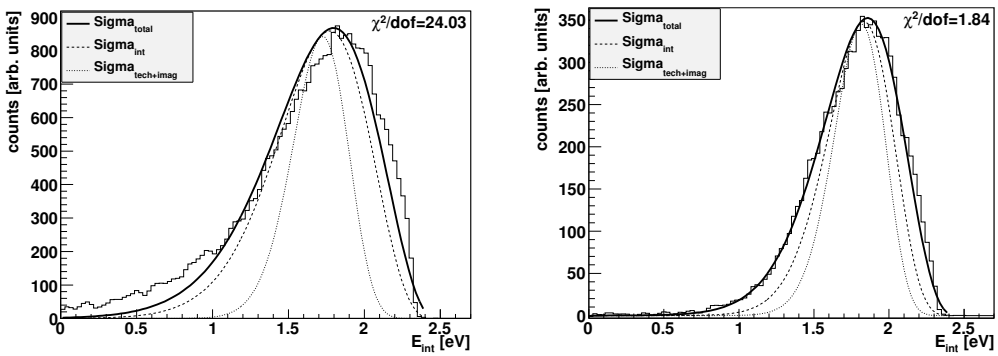

(a) Scattering angle from 0°-180°

(b) Scattering angle from 0°-45°

Figure 4.7: Fit function for 0.65 eV relative kinetic energy. No suitable result can be obtained for the fit with two isomers, so the fit for only the HCO^+ isomer is shown. The two dashed lines show the split-up of the different σ.

internal energy the broadening of the internal energy σ_{int} itself is also considered. As this uncertainty is not correlated to σ_{tech} and σ_{VMI} one can sum up all these three uncertainties

$$\sigma^2 = \sigma_{total}^2 = \sigma_{tech}^2 + \sigma_{VMI}^2 + \sigma_{int}^2 \,. \tag{4.18}$$

To find the best fit parameters a χ^2 test was used

$$\chi^2 = \sum_{i=1}^{n} \frac{(O_i - E_i)^2}{E_i}, \tag{4.19}$$

where O_i is an observed value, E_i an expected (theoretical) value and n is the number of bins[1] in the histogram. By minimizing χ^2/dof the best fit is obtained[2]. In Fig. 4.7 and 4.8 the results of the fit function for the relative kinetic energy of 0.65 eV and 1.85 eV are shown. For both energies the fit functions for either the whole scattering sphere (left plot) or mainly forward scattering (right plot) are presented. By looking at the fit parameters χ^2/dof of both plots (left and right), one can see that the results for the forward scattering is better (lower χ^2/dof value). This can be explained by the fact that in the fit function only forward scattering was considered.

[1]The plots in Fig. 4.7 and 4.8 are divided into n bins, where for each bin the number of counts is depicted.

[2]$dof \mathrel{\hat{=}}$ degrees of freedom = bins - fit parameters

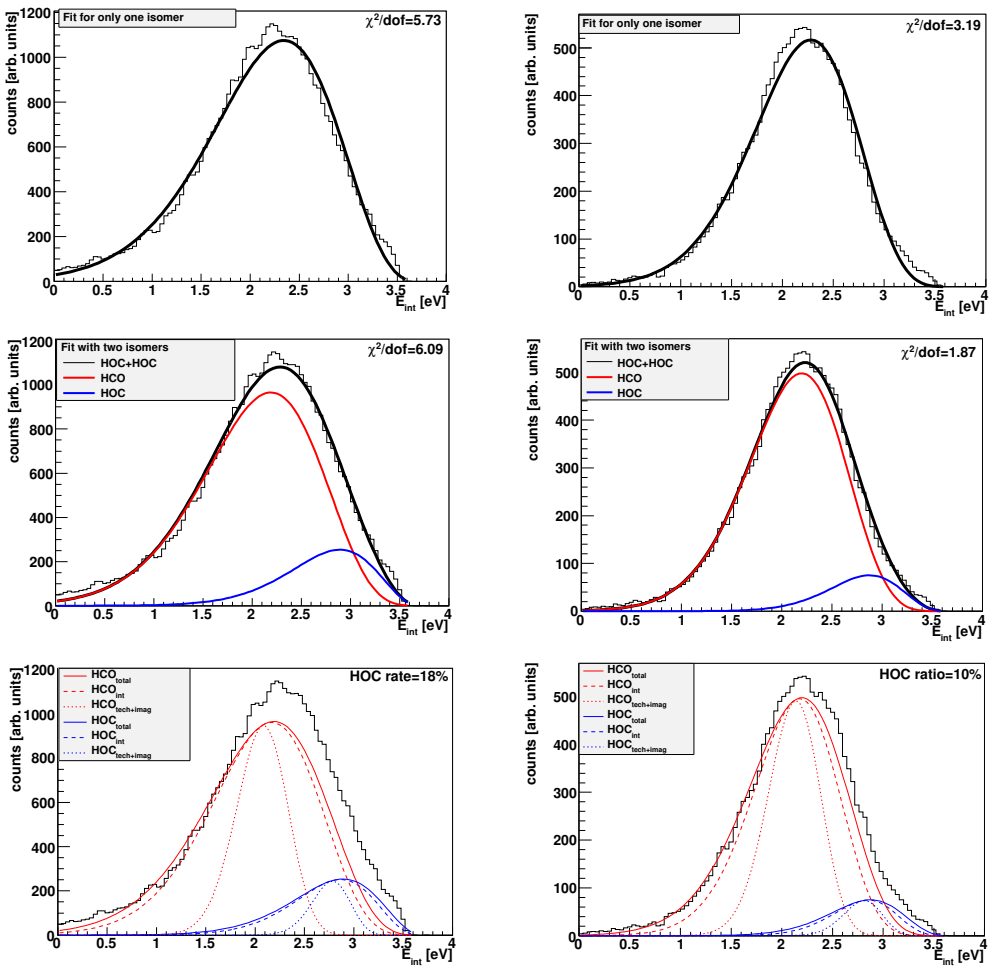

(a) Scattering angle from 0°-180°

(b) Scattering angle from 0°-45°

Figure 4.8: Fit functions for 1.85 eV relative kinetic energy. The left plots are for the whole scattering angle and the right ones consider only forward scattering. The two plots at the top show the fit function with no appearance of the HOC^+ isomer. The middle ones are the fit functions for both isomers, where the lower plots show the split-up of the σ (see text for more details).

To determine the ratio of the two isomers with the fit function, exemplarily the reaction with the collision energy of 0.65 eV and 1.85 eV, respectively, are considered. The fitting of the internal energy distribution for the 0.65 eV collision results in a HOC^+ ratio of 0. A reason for this is that HOC^+ is only possible above 1.6 eV, because the enthalpy of the reaction channels are different by this value. By assuming that the internal energy distribution for the HOC^+ isomers looks similar than the distribution of the HCO^+ isomer, almost no contribution is left for the HOC^+ isomer. For the energies of 2.5 eV and 4.4 eV no fit function is made. As discussed in section 2.2 the transition state from $HCO^+ \longleftrightarrow HOC^+$ is 3.1 eV beyond the energy level of the HCO^+. Thus, it is not possible to distinguish between the two isomers when the internal energy is higher than this value.

In Fig. 4.8 the fit with the two isomers is shown for the collision with 1.85 eV kinetic energy (middle plot). By looking at the forward scattering one can see that the fit parameter χ^2/dof is better for the fit with two isomers. The two coloured lines in the middle plot represent the two different isomers, where the red one is the HCO^+ isomer and the blue one the HOC^+. The height of the two isomers depict the parameters A and B (compare equation (4.14) and (4.16)). The percentage for the HOC^+ isomer is calculated by

$$\frac{B}{A+B} \cdot 100\% \,. \tag{4.20}$$

The dashed lines in Fig. 4.7 and 4.8 (lower plot) represent the contribution of the different uncertainties ($\sigma_{tech+VMI}$, σ_{int}), where σ_{tech} and σ_{VMI} are determined as described in section 3.3 and σ_{int} is a parameter of the fit function and calculated by that. The values are shown in Tab. 4.4.

Table 4.4: Split-up of the σ as shown in Fig. 4.7 and 4.8.

energy	angle [°]	σ_{tech} [m/s]	σ_{VMI} [m/s]	σ_{int} [m/s]
0.65 eV	0-180	83	39	123
	0-45			92
1.85 eV (one isomer)	0-180	58	37	171
	0-45			128
1.85 eV (two isomers)	0-180	58	37	149
	0-45			114

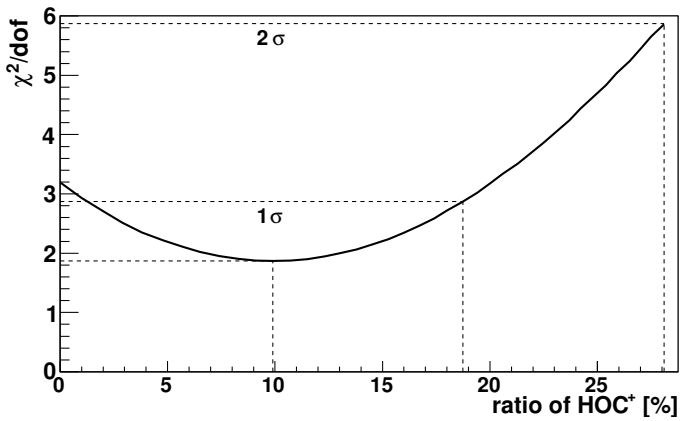

Figure 4.9: Quality of the fit function χ^2 as a function of the HOC^+ ratio with the $1\,\sigma$ and $2\,\sigma$ error range.

As can be derived from the different contributions, the width of the curve is mainly given by σ_{int}. This is explained by the fact that the internal excitation after the collision is not always the same, so different vibration modes of the molecules are excited. One can also see that the width of the internal excitation is higher if one takes the whole scattering angle into account.

The fit function for the 1.85 eV relative kinetic energy measurement for forward scattering is the most interesting one. Here the fit with the second isomer leads to a better result and the transition state between the two isomers has not to be taken into account.

In Fig. 4.9 χ^2/dof is plotted as a function of the HOC^+ ratio. One can see a minimum at 10% (with $\chi^2/dof = 1.87$). With the Least Squares Method the $1\,\sigma$ error is defined as $\Delta\chi^2 = +1$ above the best-fit point and the two sigma error range corresponds to $\Delta\chi^2 = +4$. By taking the $1\,\sigma$ error range an upper limit of about 19% for the HOC^+ isomer can be obtained and for a 28% ratio of the HOC^+ isomer the error is still in the $2\,\sigma$ range.

With these results one cannot exclude that only the HCO^+ isomer is produced, but one can definitely say that the ratio for the isomer HOC^+ of 50% as suggested by Klippenstein and coworkers is not obtained. This result is interesting as it shows that the isomerisation process is probably influencing the ratio even at high relative energies.

4.3 $HOCO^+ + CO$

In the second experiment we analyse the reaction

$$HOCO^+ + CO \rightarrow HCO^+ + CO_2 \qquad (\Delta H = -0.56\text{eV}) \tag{4.21}$$

which also forms the isomer HOC^+ under endothermic conditions

$$HOCO^+ + CO \rightarrow HOC^+ + CO_2 \qquad (\Delta H = +1.18\text{eV})\,. \tag{4.22}$$

Due to the endothermic reaction for the isomer HOC^+ the energy barrier of 1.18 eV has to be exceeded to form this isomer. In the previous reaction (H_3^++CO) this is not the case. There both isomers can be produced because both reaction channels are exothermic. Therefore we choose two relative kinetic energies where one is lower than the barrier and one is higher. As described in section 3.1 the $HOCO^+$ cations are produced in the ion trap by the collision of CO_2 and H_3^+. This beam is then accelerated towards the scattering chamber. By changing the offset voltage of the scattering region the energy of the ion beam can be controlled. The ion energies for the two experiments are depicted in Tab. 4.5.

Table 4.5: Table of the $HOCO^+$ ion energies used in the experiment. The mean values and the sigmas are shown as well well as the relative energies of the two reactant beams.

energy [meV]	σ [meV]	E_{rel} [eV]
2 560	171	0.8
4 840	158	1.7

4.3.1 Gaussian calculations towards determining the enthalpy and isomerisation

For the reactions 4.21 and 4.22 no calculations for the transition state in the $OCO\cdots HCO^+$ intermediate complex can be found in literature. Such calculations are of interest, because they can show if an isomerisation between the complexes is possible as in the previous reaction. To determine the energy for this transition state and the enthalpy difference for the two reaction channels with the products HCO^+ and HOC^+, the G09 software has been implemented [77]. The calculations are carried out using the Møller-Plesset perturbation theory

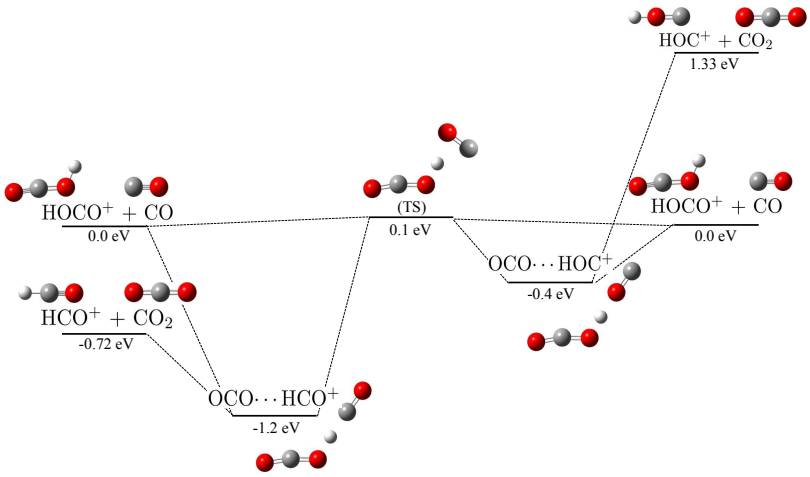

Figure 4.10: Potential energy surface (PES) for the reaction HOCO$^+$+CO→HCO$^+$/HOC$^+$+CO$_2$. The PES is calculated at a MP2 level with a 6-311++G** basis set (red = oxgygen, gray = carbon, white = hydrogen).

(MP2) at the 6-311++G** level of theory. The energies for all the components in reaction

$$\mathrm{HOCO^+ + CO \rightarrow HCO^+/HOC^+ + CO_2 + \Delta H} \tag{4.23}$$

are calculated by optimizing the geometry (angles and bond lengths) of the molecules.

In Fig. 4.10 the calculated potential energy surface is presented with the energies for the two intermediate complexes OCO$\cdots$HCO$^+$ and OCO$\cdots$HOC$^+$. The transition state of these two intermediate complexes is presented as well. One can see that the transition state is just 0.1 eV above the zero-energy level of the reactants.

To calculate the energy levels of the intermediate complexes, the geometry of the involved molecules is first optimized. These optimized molecules are then scanned in the sense of distance, angle and minimal energy for each structure.

By comparing the energies of all the reaction components of reaction 4.23, the enthalpy for the HCO$^+$ channel of $\Delta H_1 =$ -0.72 eV and for the HOC$^+$ channel $\Delta H_2 = 1.33$ eV are obtained. The energy difference for the two channels is ΔH_2 - $\Delta H_1 = 2.05$ eV. Comparing this value with the proton affinity and the results of Li and coworkers, an inaccuracy of $\sim 20\%$ can be approximated [19].

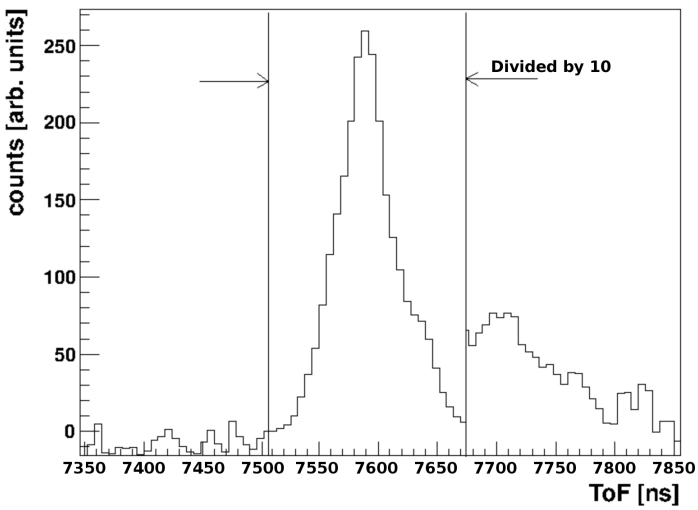

Figure 4.11: Time of flight of the HOCO experiment with 0.8 eV relative energy. One can see that there is no peak on the left side of the main peak. Thus, no CO^+ was determined. The $H^{13}CO^+$ peak still exists.

Even with this accuracy of the calculation the transition state between the two complexes is below or only a few 100 meV above the zero energy of $HOCO^+$ + CO. For a reaction with a relative energy of only 0.5 eV this transition state can be passed and an isomerisation process is possible.

4.3.2 Time of flight spectrum

As already discussed in section 4.2.1 the time of flight spectrum shows different peaks for mass 28 amu, 29 amu, 30 amu and also 31 amu, where m = 29 amu corresponds to the HCO^+ and HOC^+ cations. In Fig. 4.11 one can see the time of flight spectrum for the $HOCO^+$+CO experiment at 0.8 eV relative energy. The main peak in the middle corresponds again to the HCO^+ molecules with m = 29 amu. On the right side of the main peak at m = 30 amu appears the peak of the $H^{13}CO^+$ molecules. The peak for the CO^+ molecules, which was clearly detected in the previous experiments (especially for higher collision energies), does not appear in this TOF measurement. In the discussion of the TOF spectrum in section 4.2.1 (H_3^++CO) the possibility that the CO^+ is produced in the neutral beam source was mentioned. Due to the fact that no CO^+ peak appears in the TOF measurement of this reaction, one can exclude this possibility. If one compares this TOF spectrum with the TOF spectrum of the H_3^++CO reaction

(see Fig. 4.2(a)), a shift of $\sim$80 ns and a broader peak for the HCO^+ can be seen. It is unclear where this effect comes from, but simulation with SIMION show a shift of the time of flight of 80 ns if the potential of the repeller plate is decreased by 15 V. A second effect of the lower potential of this plate is a higher standard deviation what explains the more expanded peak. Another reason could be a different spatial interaction region of the two beams in this experiment, as this can also lead to a different time of flight.

4.3.3 3D-Velocity images and angular dependence

In section 4.2.2 it is described how the radial velocity is calculated. In Fig. 4.12 (left image) the 3D scattering images for the two collision energies are shown. As already observed in the previous experiment the main part of the ions are scattered in forward direction. The red circle depicts again the kinematic cut-off of the reaction and the dashed white circles show each an energy loss of 1 eV. Again, a huge internal excitation can be observed for both energies so that no ions are scattered to the kinematic cut-off.

If one looks at the angle dependence of the internal energy (Fig.4.12, right) it is evident that for larger scattering angles the internal energy is higher. This is the same result than in the H_3^++CO experiment and one can also see that for higher relative energies the angle dependence is higher.

4.3.4 Internal excitation of the products

In the right plots of Fig. 4.12 one can see the internal energy after the collision. As described in section 4.2.4 the internal energy is the difference of the kinematic energies before and after the collision with respect of the enthalpy.

Comparing the internal energy with respect to the maximal available energy (E_{kin}-ΔH) from the previous reaction (H_3^++CO) with the results of the present measurement, one can see that the present internal energy shows less excitation. This can be caused by the difference of the enthalpies of the two reactions or by the fact that the educts of the two reactions are different. The H_2 molecule in the previous reaction has very high vibrational energies in low excited states (1.36 eV at $\nu = 2$) and in the current reaction the second educt is the CO_2 molecule with lower vibrational energies as shown in Tab. 4.6.

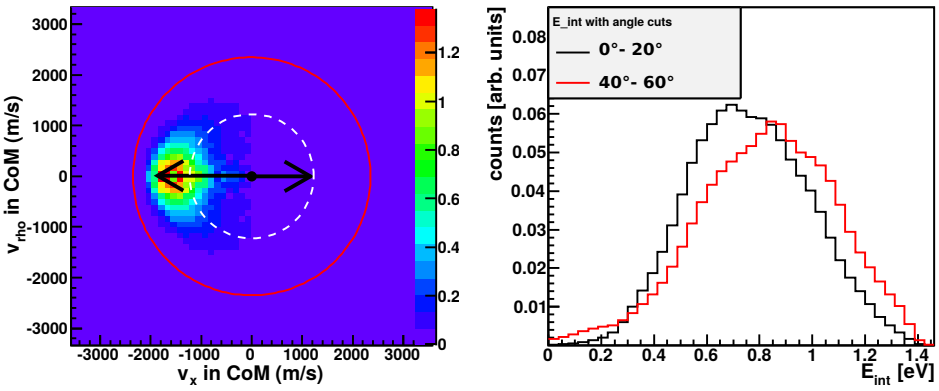

(a) **0.8 eV**

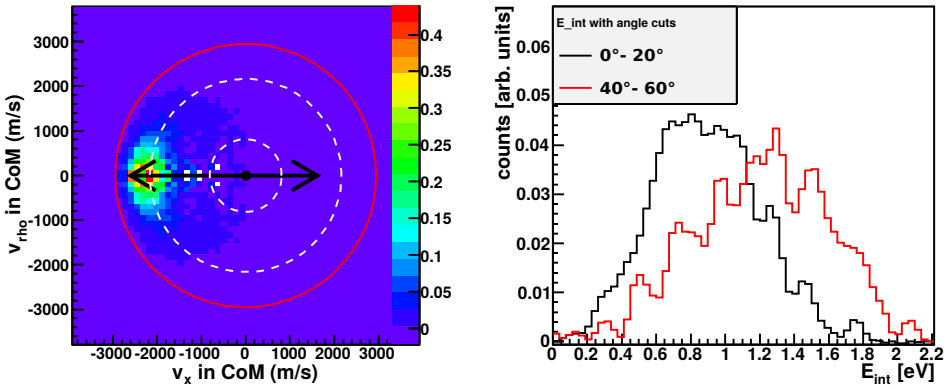

(b) **1.7 eV**

Figure 4.12: 3D-velocity images of the HOCO$^+$ eperiment (left) and the internal energy distribution (right) for both relative energies.

Table 4.6: Vibration energies of the CO_2 molecule with symmetric and anti-symmetric stretch as well as the bending mode [60].

Mode	Freq. (cm^{-1})	Energy (eV)
sym. stretch	1 333	0.165
asym. stretch	2 349	0.291
bend	667	0.083

As Hirano and coworkers tell, the departing H_2 carries away 2/3 of the excess energy [44]. This could explain the difference in the internal energy distribution between both experiments as in the second experiment no H_2 molecules are available.

4.3.5 Ratio of HOC^+ / HCO^+

In the reaction H_3^++CO both isomers HCO^+ and HOC^+ can be produced with small relative energies because both reaction channels are exothermic. A clear separation of the two isomers is not possible, but a fit is made to obtain a upper bound for the HOC^+ isomer. In the present reaction ($HOCO^+$+CO) up to a relative kinetic energy of 1.33 eV no HOC^+ can appear because the endothermicity for creating this isomer is not reached. This is quite interesting, because one knows that the internal energy of a reaction below this limit always shows just one channel.

By comparing the shape of the internal energy distribution of the two different reactions one may tell more about the HOC^+ ratio in the first experiment. The shape of E_{int} for the 0.8 eV ($HOCO^+$) reaction is similar to the shape for the 1.85 eV and 2.5 eV (H_3^+) reaction. In the fit for the H_3^++CO experiment with 1.85 eV relative energy the right part of the distribution was declared to be the part of the second isomer HOC^+. As the shape is now the same for the current experiment at 0.8 eV relative kinetic energy where no HOC^+ can be produced, it is questionable if this comparison can be done. A more detailed analysis of the ratio in the $HOCO^+$ experiment could help to make more precise predictions.

Chapter 5

Conclusion

In the present master thesis the ratio of the isomers HCO^+ and HOC^+, formed by proton transfer reactions, is studied. Our data analysis for the system including a fit function for two isomers shows an upper limit of 19% for the HOC^+ isomer in the reaction

$$H_3^+ + CO \rightarrow HCO^+/HOC^+ + H_2\,,$$

with a relative kinetic energy of the two reactants of 1.85 eV. This is not in agreement with the prediction of Klippenstein and coworkers who claim this ratio should increase up to 50% for relative energies above 1 eV [45]. Due to the high internal excitation of the products, the energy resolution of the two channels does not afford to separate the two peaks of the different isomers. Thus, no precise ratio of the isomers can be determined.

In the second proton transfer reaction

$$HOCO^+ + CO \rightarrow HCO^+/HOC^+ + CO_2\,,$$

which is studied in this thesis, the internal excitation of the products leads to a similar energy resolution and no separation of the two isomers is possible. The ratio of the HOC^+ isomer is determined to be below 50%

This experiment presents the first results of a velocity map imaging process concerning the investigated reactions and opens the possibility for obtaining complete dynamical and kinematical pictures for ion-molecule reaction systems of interest for astrochemistry.

Chapter 6

Outlook

In the previous chapters the results for the reactions H_3^++CO and $HOCO^+$+CO have been discussed. For the HOC^+ ratio an upper limit of 19% was obtained, however it is also possible that the HCO^+ ratio is 100%. The limiting property for a good separation of the two isomers is the energy resolution. Thus, the exact ratio for the two product isomers HCO^+ and HOC^+ remains unclear and one can only predict an upper and lower limit for the HOC^+ ratio to be 19% and 0% respectively. A reason for the limiting energy resolution is on the one hand the high internal excitation with a high width and on the other hand the distance between the two isomers is too small to detect a clear ratio.

In this chapter, I will give a brief outlook for possible experimental improvements and new planed related reactions to the studied system towards understanding the HCO^+/HOC^+ ratio as a function of the relative energy are presented.

6.1 Technical improvements

One important question relies on the possibility of resolving both isomeric reaction channels. There are four parameters influencing the resolution of the two isomers. The first improvement can be achieved for the reactant ion beam. Recently it has been found out, that by using additional lenses after the ion trap, the energy resolution of the ion beam can be increased at least by factor 2. A second improvement for the velocity of the reactant species relies on the temperature of the neutral molecular CO beam. Pre-cooling of the gas before entering the valve through collisions with buffer gas together with higher backing

pressure will lower the temperature of the supersonic beam and therefore also the velocity distribution will be improved. One has to take into account that a higher pressure before the valve and the pre-cooling of the CO gas will lead to cluster formation.

By reducing the uncertainty of the VMI spectrometer (σ_{VMI}) the resolution will be improved as well. This can be achieved by minimizing the interaction volume of both reactant beams. These three improvements can generally be done, though they do not maintain to a much better resolution of the internal energy, as the part of the VMI spectrometer uncertainty is little.

A lower internal excitation of the products will lead to a better separation of the two isomers. As discussed in section 4.2.4, the internal excitation relies on the intrinsic physical characteristics of the system and cannot be improved. As the uncertainty of the internal energy σ_{int} is the main contribution to the told uncertainty, it will be difficult to separate efficiently the two isomers of the reaction H_3^++CO. To investigate in the branching ratio HCO^+/HOC^+ other reactions are of interest and will be presented in the next section.

6.2 Possible experiments

As the energy distance between the two isomers is too low to separate them, it would be of interest to have different scattering dynamics. By exchanging the hydrogen by deuterium one gets the reaction

$$D_3^+ + CO \rightarrow DCO^+/DOC^+ + D_2 \tag{6.1}$$

which also leads to two different isomers.

Due to the mass difference of the H_2 and D_2 molecules, which are produced in the reaction as well, one can say that the vibrational frequencies of the D_2 molecule will be lower than of the H_2 molecule. The classical vibrational frequency ν is related to the reduced mass μ and the force constant k by

$$\nu = \frac{1}{2\pi}\left(\frac{k}{\mu}\right)^{1/2} \tag{6.2}$$

so it scales with $\mu^{-1/2}$. In section 4.2.4 a reason for the high internal excitation of the reaction H_3^++CO was indicated as the vibrational energy of the H_2 molecule

which could be improved in the reaction (6.1) by the double mass of deuterium.

Another interesting reaction to investigate is the reaction

$$DH_2^+ + CO \rightarrow DCO^+/HCO^+ + H_2/DH \tag{6.3}$$

which was investigated by Yu theoretically [20]. Here the competition between the proton and deuterium transfer could be investigated. Yu calculated a stronger decrease of the DCO^+ ratio with temperature than the HCO^+ ratio. Thus a higher ratio of DCO^+/DOC^+ than HCO^+/HOC^+ can be obtained at relative collision energies of about 1 eV.

Two other reactions which could be studied are:

$$C^+ + H_2O \rightarrow HCO^+/HOC^+ + H \tag{6.4}$$

and

$$CO^+ + H_2 \rightarrow HCO^+/HOC^+ + H \tag{6.5}$$

which were studied in the past by using a selected-ion flow-tube mass spectrometer by Freeman and coworkers [39]. In their measurements they yielded HCO^+/HOC^+ ratios of 0.19 and 1.08 for reaction (6.4) and (6.5) respectively. These ratios, especially for reaction (6.5), makes it easier to separate the two isomers. Another big advantage of these two reactions is that the neutral product is just a hydrogen atom and no kinetic energy can be transfered into vibrations of this product. Therefore, lower excitation is expected in this system. This would lead to a better energy resolution and to a higher separation of the peaks of the two isomers (see section 4.2.4).

Regarding the reaction $HOCO^+ + CO$ an interesting question is, if in this reaction only a proton transfer takes place or if there is also an oxygen transfer. By replacing CO by its isotopic isomer ^{13}CO the reactions

$$HOCO^+ + {}^{13}CO \rightarrow H^{13}CO^+ + CO_2 \tag{6.6}$$

and

$$HOCO^+ + {}^{13}CO \rightarrow HCO^+ + {}^{13}CO_2 \tag{6.7}$$

can take place, where the masses of the produced ions differ in 1 amu.

Producing the $H^{18}OC^{18}O^+$ ion (instead of $HOCO^+$) with the isotopic isomer $C^{18}O_2$ would lead to the reactions

$$H^{18}OC^{18}O^+ + CO \rightarrow HC^{18}O^+ + CO^{18}O \tag{6.8}$$

and

$$H^{18}OC^{18}O^+ + CO \rightarrow HCO^+ + C^{18}O_2 \tag{6.9}$$

where the masses of the produced ions differ even in 2 amu.

Although the two isomers in our investigated reactions could not be separated in a clear way, there are a lot of interesting questions involving proton transfer reactions which are waiting to be studied.

Bibliography

[1] E. Herbst. Chemisty in the interstellar Medium. *Annual Review of Phys*, 46:27–54, 1995.

[2] M. Larsson, W. D. Geppert, and Nyman G. Ion chemistry in space. *Reports on Progress in Physics*, 75:066901, 2012.

[3] E. Roueff and E. Herbst. Molecular ions in astrophysics. *Journal of Physics: Conference Series*, 192:012008s, 2009.

[4] S. D. Doty, E. F. van Dishoeck, F. F. S. van der Tak, and A. M. S. Boonman. Chemistry as a probe of the structures and evolution of massive star forming regions. *Astronomy and Astrophysics*, 389:446–463, 2002.

[5] F. Herpin, J. R. Goicoechea, J. R. Pardo, and J. Cernicharo. Chemical evolution of circumstellar envelopes of carbon rich post asymptote giant branch objects. *The Astrophysical Journal*, 577:961, 2002.

[6] V. Vuitton, R. V. Yelle, and M. J. McEwan. Ion chemistry and n-containing molecules in titan's upper atmosphere. *Icarus*, 191:722 – 742, 2007.

[7] W. D. Geppert, M. Hamberg, R. D. Thomas, F. Osterdahl, F. Hellberg, V. Zhaunerchyk, A. Ehlerding, T. J. Millar, H. Roberts, J. Semaniak, M. af Ugglas, A. Kallberg, A. Simonsson, M. Kaminska, and M. Larsson. Dissociative recombination of protonated methanol. *Faraday Discuss.*, 133:177–190, 2006.

[8] E. Vigren, M. Hamberg, V. Zhaunerchyk, M. Kaminska, J. Semaniak, M. Larsson, R. D. Thomas, M. af Ugglas, I. Kashperka, T. J. Millar, C. Walsh, H. Roberts, and W. D. Geppert. Dissociative recombination of protonated formic acid: Implications for molecular cloud and cometary chemistry. *The Astrophysical Journal*, 709:1429, 2010.

[9] A. G. Tielens. Interstellar polycyclic aromatic hydrocarbon molecules. *Annual Review of Astronomy and Astrophysics*, 46:289–337, 2008.

[10] J. J. Thomson. Rays of positive electricity. *Proceedings of the Royal Society A*, 89:1–20, 1913.

[11] T. R. Hogness and E. G. Lunn. The ionization of hydrogen by electron impact as interpreted by positive ray analysis. *Phys. Rev.*, 26:44–55, 1925.

[12] D. W. Martin, E. W. McDaniel, and M. L. Meeks. On the Possible Occurence of H_3^+ in Interstellar Space. *Astrophysical Journal*, 134:1012–1013, 1961.

[13] W. D. Watson. The rate of formation of interstellar molecules by ion-molecule reactions. *The Astrophysical Journal*, 183:L17–L20, 1973.

[14] T. R. Geballe and T. Oka. Detection of H_4^+ in interstellar space. *Nature*, 384:334–335, 1996.

[15] E. Herbst. The Astrochemistry of H_3^+. *Philosophical Transactions of the Royal Society A*, 358:2523–2534, 2000.

[16] D. Buhl and L.E. Snyder. Unidentified interstellar microwave line. *Nature*, 228:267–269, 1970.

[17] N.G. Adams and D. Smith. The selected ion flow tube (sift): a technique for studying ion-neutral reactions. *International Journal of Mass Spectrometry and Ion Physics*, 21:349–359, 1976.

[18] R. Wester. Radiofrequency multipole traps: Tools for spectroscopy and dynamics of cold molecular ions. *Journal of Physics B*, 42:154001, 2009.

[19] H. Li, T. Hirano, T. Amano, and R. Roy. Pathways and reduced-dimension five-dimensional potenital energy surface for the reaction H_3^++CO→HCO^+ and H_3^++CO→HOC^+. *The Journal of Chemical Physics*, 129:244306, 2008.

[20] H. Yu. Product branching ratios of the reaction of CO with H_3^+ and $H2D^+$. *The Astrophysical Journal Letters*, 706:L52, 2009.

[21] H. Le, T. J. Frankcombe, and M. A. Collins. Reaction dynamics of H_3^+ + CO on an interpolated potential energy surface. *The Journal of Physical Chemistry A*, 114:10783–10788, 2010.

[22] H. Masso and L. Wiesenfeld. The HCO^+H_2 van der waals interaction: Potential energy and scattering. *The Journal of Chemical Physics*, 141:184301, 2014.

[23] W. Herbst, E.; Klemperer. The formation and depletion of molecules in dense interstellar clouds. *Astrophysical Journal*, 185:505, 1973.

[24] R. C. Woods, C. S. Gudeman, R. F. Goldsmith, G. R. Huguenin, W. M. Irvine, A. Hjalmarson, L.-A. Nyman, and H. Olofsson. The HCO^+/HOC^+ abundance ratio in molecular clouds. *Astrophysical Journal*, 270:583–588, 1983.

[25] A. J. Apponi and L. M. Ziurys. New observations of the [HCO^+]/[HOC^+] ratio in dense molecular clouds. *The Astrophysical Journal*, 481:800–808, 1997.

[26] M. A. Smith, S. Schlemmer, J. von Richthofen, and D. Gerlich. $HOC^+ + H_2$ isomerization rate at 25 K: Implications for the observed HCO^+/HOC^+ ratios in the interstellar medium. *The Astrophysical Journal Letters*, 578:L87, 2002.

[27] H. Liszt, R. Lucas, and J. H. Black. The abundance of HOC^+ in diffuse clouds. *Astronomy and Astrophysics*, 428:117, 2004.

[28] *IUPAC. Compendium of Chemical Terminology, 2nd ed. (the "Gold Book").* Blackwell Scientific Publications, Oxford 1997.

[29] E. S. Wirstrom, C. M. Persson, A. Hjalmarson, J. H. Black, P. Bergman, W. D. Geppert, M. Hamberg, and E. Vigren. Observational constraints on the formation of interstellar methanol. In *Organic Matter in Space Proceedings IAU Symposium*, volume 251, 2008.

[30] B. M. Jones, F. Zhang, R. I. Kaiser, A. Jamal, A. M. Mebel, M. A. Cordiner, and S. B. Charnley. Formation of benzene in the interstellar medium. *Proceedings of the National Academy of Sciences of the United States of America*, 2010.

[31] C. Pirim and L. Krim. An FTIR study on the catalytic effect of water molecules on the reactionof CO successive hydrogenation at 3 K. *Chemical Physics*, 380, 2011.

[32] R. Wester. Velocity map imaging of ion-molecule reactions. *Phys. Chem. Chem. Phys.*, 16:396–405, 2014.

[33] W. Klemperer. Carrier of the interstellar 89.190 GHz line. *Nature*, 227:1230, 1970.

[34] T. J. Millar, A. Bennett, J. M. C. Rawlings, P. D. Brown, and S. B. Charnley. Gas phase reactions and rate coefficients for use in astrochemistry - THE UMIST ratefile. *Astronomy and Astrophysics Supplement Series*, 87:585–619, 1991.

[35] E. Herbst, J. M. Norbeck, P. R. Certain, and W. Klemperer. Interstellar COH^+. *Astrophysical Journal*, 207:110–112, 1976.

[36] L. M. Ziurys and A. J. Apponi. Confirmation of interstellar HOC^+: Reevaluating the HCO^+/HOC^+ abundance ratio. *The Astrophysical Journal Letters*, 455:L73, 1995.

[37] C. Savage and L. M. Ziurys. Ion chemistry in photon-dominated regions: Examining the $HCO^+/HOC^+/CO^+$ chemical network. *The Astrophysical Journal*, 616:966, 2004.

[38] D. A. Dixon, A. Komornicki, and W. P. Kraemer. Energetics of the protonation of CO: Implications for the observation of HOC^+ in dense interstellar clouds. *The Journal of Chemical Physics*, 81:3603–3611, 1984.

[39] C. G. Freeman, J. S. Knight, J. G. Love, and M. J. McEwan. The reactivity of HOC^+ and the proton affinity of CO at O. *International Journal of Mass Spectrometry and Ion Processes*, 80:255–271, 1987.

[40] D. J. DeFrees, J. Stephen Binkley, and A. D. McLean. The quantum mechanical calculation of rotational spectra. a comparison of methods for C_2H_2, HCN, HNC, HCO^+, N_2H^+, CO, and N_2. Predictions for $HCNH^+$, COH^+, HBO, HBNH, and HBF^+. *The Journal of Chemical Physics*, 80:3720–3725, 1984.

[41] M. F. Jarrold, M. T. Bowers, D. J. Defrees, A.D. McLean, and E. Herbst. A reanalysis of the HCO^+/HOC^+ abundance ratio in dense interstellar clouds. *Astrophysical Journal*, 303:392–400, 1986.

[42] E. Herbst and D. E. Woon. Erratum: "why HOC^+ is detectable in interstellar clouds: The rate of the reaction between HOC and H_2" (apj, 463, l113 [1996]). *The Astrophysical Journal Letters*, 471:L73, 1996.

[43] D. E. Woon. An abinitio benchmark study of the H+CO $\rightarrow$ HCO reaction. *The Journal of Chemical Physics*, 105:9921–9926, 1996.

[44] T. Hirano, H. Li, R.J. Le Roy, and T. Amano. Intermolecular Vibrational Energy Redistribution in the Reaction H_3^++CO$\rightarrow$$HCO^+/HOC^+$. Ohio State University, 2009. http://hdl.handle.net/1811/37971.

[45] S. J. Klippenstein, Y. Georgievskii, and B. J. McCall. Temperature dependence of two key interstellar reactions of H_3^+: O(3P) + H_3^+ and CO + H_3^+. *The Journal of Physical Chemistry A*, 114:278–290, 2010.

[46] R. C. Woods, T. A. Dixon, R. J. Saykally, and P. G. Szanto. Laboratory microwave spectrum of hco^+. *Phys. Rev. Lett.*, 35:1269–1272, Nov 1975.

[47] C. S. Gudeman and R. C. Woods. Experimental detection of hoc^+ by microwave spectroscopy. *Phys. Rev. Lett.*, 48:1768–1768, Jun 1982.

[48] A. J. Illies, M. F. Jarrold, and M.T. Bowers. On the formation of HCO^+ and HOC^+ from the reaction between H_3^+ and CO. *The Journal of Chemical Physics*, 77:5847–5848, 1982.

[49] M. J. McEwan. *Advances in Gas Phase Ion Chemistry*, volume 1. (Greenwich: JAI), 1992.

[50] R. Wester, U. Hechtfischer, L. Knoll, M. Lange, J. Levin, M. Scheffel, D. Schwalm, A. Wolf, A. Baer, Z. Vager, D. Zajfman, M. Mladenovi, and S. Schmatz. Relaxation dynamics of deuterated formyl and isoformyl cations. *The Journal of Chemical Physics*, 116:7000–7011, 2002.

[51] A. T. J. B. Eppink and D. H. Parker. Velocity map imaging of ions and electrons using electrostatic lenses: Application in photoelectron and photofragment ion imaging of molecular oxygen. *Review of Scientific Instruments*, 68:3477–3484, 1997.

[52] R. Otto. *Dynamics of a Microsalvated Ion-Molecule Reaction.* PhD thesis, Universität Freiburg, 2011.

[53] M. Stei. Dreidimensionale Abblildung von Ion-Molecule-Reaktionen. Master's thesis, Universität Freiburg, 2009.

[54] J. Mikosch. *Dynamics of anion-molecule reactions at low energy.* PhD thesis, Universität Freiburg, 2007.

[55] J. Mikosch, U. Fruhling, S. Trippel, D. Schwalm, M. Weidemuller, and R. Wester. Velocity map imaging of ion-molecule reactive scattering: The $Ar^+ + N_2$ charge transfer reaction. *Phys. Chem. Chem. Phys.*, 8:2990–2999, 2006.

[56] J. Mikosch, S. Trippel, R. Otto, C. Eichhorn, P. Hlavenka, M. Weidemller, and R. Wester. Kinematically complete reaction dynamics of slow ions. *Journal of Physics: Conference Series*, 88:012025, 2007.

[57] W. C. Wiley and I. H. McLaren. Time-of-flight mass spectrometer with improved resolution. *Review of Scientific Instruments*, 26:1150–1157, 1955.

[58] D. Gerlich. Inhomogeneous rf fields: A versatile tool for the study of processes with slow ions. *Advances in Chemical Physics*, 82:1–176, 1992.

[59] W. Christen, K. Rademann, and U. Even. Efficient cooling in supersonic jet expansions of supercritical filuids: CO and CO_2. *The Journal of Chemical Physics*, 125:174307, 2006.

[60] E. W. Lemmon, M. O. McLinden, and D. G. Friend. in NIST Chemistry WebBook, NIST Standard Reference Database Number 69, edited by P.J. Linstrom and W.G. Mallard, June 2005 (National Institute of Standards and Technology, Gaithersburg, MD, 2005).

[61] S. Trippel. *Aligned Molecules for Reactive Scattering.* PhD thesis, Universität Freiburg, 2010.

[62] S. Trippel, M. Stei, C Eichhorn, R Otto, P Hlavenka, M. Weidemuller, and R Wester. Nanosecond photofragment imaging of adiabatic molecular alignment. *The Journal of Chemical Physics*, 134:104306, 2011.

[63] SIMION Ion Optic Simulation Software Version 8.0, Indaho National Engineering Laboratory, 2006.

[64] M. Stei, J. von Vangerow, R. Otto, A. H. Kelkar, E. Carrascosa, T. Best, and R. Wester. High resolution spatial map imaging of a gaseous target. *The Journal of Chemical Physics*, 138:214201, 2013.

[65] B. Whitacker. *Imaging in Melecular Dynamics: Technology an Application.* Cambridge University Press, 2003.

[66] W. Demtröder. *Molekülpyhsik: theoretische Grundlagen und experimentelle Methoden.* Oldenbourg Wissenschaftsverlag, 2003.

[67] J. S. Coursey, D. J. Schwab, J. J. Tsai, and R. A. (2010) Dragoset. National Institute of Standards and Technology, Gaithersburg, MD. Atomic Weights and Isotopic Compositions (version 3.0). Available: http://physics.nist.gov/Comp [2014, October 24].

[68] G. L. Weissler, J. A. R. Samson, M. Ogawa, and G. R. Cook. Photoionization analysis by mass spectroscopy. *Journal of the Optical Society of America*, 49:338, 1959.

[69] S. Trippel, M. Stei, J. A. Cox, and R. Wester. Differential Scattering Cross-Sections for the Different Product Vibrational States in the Ion-Molecule Reaction $Ar^+ + N_2$. *Phys. Rev. Lett.*, 110:163201, 2013.

[70] R. Candori, S. Cavalli, F. Pirani, A. Volpi, D. Cappelletti, P. Tosi, and D. Bassi. Structure and charge transfer dynamics of the $(Ar\text{-}N_2)^+$ molecular cluster. *The Journal of Chemical Physics*, 115:8888–8898, 2001.

[71] Data from NIST Standard Reference Database 69: NIST Chemistry WebBook. Available: http://webbook.nist.gov/cgi/cbook.cgi?ID=C2597446&Mask=800 [2014, October 28].

[72] S. Stamatiadis, S.C. Farantos, H. Keller, and R. Schinke. Saddle-node states in the spectra of HCO and DCO: a periodic orbit classification of vibrational levels. *Chemical Physics Letters*, 344:565 – 572, 2001.

[73] H. J. Werner, C. Bauer, P. Rosmus, H. M. Keller, M. Stumpf, and R. Schinke. The unimolecular dissociation of HCO: I. oscillations of pure CO stretching resonance widths. *The Journal of Chemical Physics*, 102:3593–3611, 1995.

[74] Data from NIST Standard Reference Database 69: NIST Chemistry WebBook. Available: http://webbook.nist.gov/cgi/cbook.cgi?ID=C17030749&Mask=800 [2014, October 24].

[75] K. P. Huber and G. Herzberg. *Molecular Spectra and Meolecular Structures; IV. Constants of Diatomic Molecules.* Van Nostrad Reinhold Company, 1979.

[76] R. C. Woods, R. J. Saykally, T. A. Dixon, P. G.Szanto, and T. G. Anderson. In *Columbus Conf.*, 1976.

[77] M. J. Frisch et al. Gaussian 09 Revision A.02. Gaussian Inc. Wallingford CT 2009.

Danksagung

Zuerst möchte ich mich bei meinem Betreuer in Wien, Herrn Prof. Aumayr bedanken, dass er mir die Möglichkeit gegeben hat, diese Masterarbeit in Innsbruck zu schreiben.

Ein sehr großes Dankeschön geht an Herrn Prof. Wester, bei welchem ich diese Arbeit geschrieben habe. Mit seiner fachlichen Kompetenz konnte er mir bei physikalischen Problemen immer gut helfen und speziell bei der Auswertung der Daten habe ich sehr hilfreiche Tipps von ihm erhalten. Danke Roland, dass du neben deinen vielen organisatorischen Tätigkeiten doch immer noch Zeit findest für uns Studenten da zu sein und für ein gutes Klima in der Gruppe sorgst.

Der ganzen Arbeitsgruppe (ich werde euch jetzt nicht alle von euch aufzählen) möchte ich danken, weil die Zeit mit euch eine sehr Schöne war. Ihr habt mich schon an meinem ersten Tag in Innsbruck in das Nachtleben in der Stadt eingeführt - ein Abend den ich so schnell nicht vergessen habe. Die Tatsache, dass ich an jedem Tag gerne auf die Uni gekommen bin, zeigt mir, dass ich mich bei euch wirklich wohl gefühlt habe.

Bei dir Steffen möchte ich mich für die Hilfe am Frequenzgenerator und für das Korrekturlesen bedanken. Aber nicht nur für das, sonder auch für die sportlichen Aktivitäten die wir zusammen gemacht haben, speziell die Skitour Mitte Mai.

Dugi, bei dir möchte ich mich auch für das Korrekturlesen bedanken, obwohl du mir damit noch sehr viel Arbeit beschert hast. Als ich in die Arbeitsgruppe kam, habe ich schnell gemerkt, dass ich mit generellen Fragen zur Physik bei dir richtig aufgehoben war. Sogar noch heute, als ich die Arbeit schon fertig hatte, hast du dir noch die Zeit genommen und mir wieder einmal statistische Auswerteverfahren erklärt.

Für die Erstbetreuung in den ersten Wochen möchte ich mich bei Martin[1] bedanken. Du hast mir geholfen den Lab-PC aufzusetzen. Auch später warst du dann immer willig, mir bei Problemen mit ROOT zu helfen. Das Nachmittagsbier zur Feier unseres Namenstags werde ich so schnell nicht vergessen, ebenso wenig den Abend als wir bei dir das WM Finale angeschaut hatten. Ich habe noch nie jemanden gesehen, der sich so freut, wenn sein Land Weltmeister wird. Ah ja, und vielen Dank für das Feldbett. Es hat das Übernachten im Labor etwas erträglicher gemacht.

Den größten Dank habe ich mir für den Schluss aufgehoben. Edu, du warst nicht nur der Betreuer meiner Masterarbeit sondern du warst für mich auch ein Mentor. In den unzähligen Stunden, welche wir gemeinsam im Labor verbracht haben (war es am späten Abend, am frühern Morgen oder dazwischen), haben wir nicht nur den Sternenhimmel am Monitor betrachtet, sondern auch über die wirklich wichtigen Dinge des Lebens geredet. Sachen wie das Korrekturlesen

[1] Stei

zähle ich jetzt gar nicht auf, denn das war für dich alles selbstverständlich. In dir habe ich einen echten Freund gefunden und ich freue mich schon, dich dann einmal im País Vasco besuchen zu kommen. Da bleibt mir wohl nur noch zu sagen: ¡Muchas Gracias por todo!
Dir Kiran möchte ich danken, weil ich beim Erstellen deines Geburtsgeschenkes mich sehr gut von der Arbeit entspannen konnte (die Kappe und die Handschuhe werden dir jetzt, nachdem du lesen gelernt hast, wohl nicht mehr passen)[1].

Beim Papa Jolly's möchte ich mich für die Möglichkeit bedanken, auch spät am Abend noch etwas zum Essen und Trinken zu bekommen. Ein weiterer Dank geht an die Programmieren von Gaussian, welche mit ihren Sprüchen, die bei einer erfolgereichen Rechnung erscheinen, dafür sorgten, dass auch diese Zeit etwas erträglich war.

Ein weiterer Dank geht an dich Benji. Mit dir habe ich schon während der gemeinsamen Schulzeit viel über Physik geredet und du warst dann sicher auch ein Mitgrund, warum ich mich für dieses Studium entschieden habe. Hiermit möchte ich mich nochmals für das Buch von Stephen Hawking bedanken, in dem du dich für die fünf Jahre Banknachbarschaft bedankt hast.

Elisabeth, bei dir möchte ich mich für die Zeit bedanken, welche ich im letzten Jahr nicht im Labor oder im Büro, sondern mit dir verbracht habe. Du warst ein guter Ausgleich zur Uni (auch wenn du einmal einen Samstag mit mir dort im Labor verbracht hast). Geschätzt habe ich aber auch unser Diskussionen über meine Arbeit, denn du hattest als Außenstehende einen anderen Blick über die Thematik, was mir oft weiter geholfen hat. Und vielen Dank dafür, dass du für mich da warst, wenn es mit der Arbeit mal nicht so gut gelaufen ist.

Ein Dank geht an meine drei Schwestern, speziell an Teresa, weil sie immer für mich da war und ich über vieles mit ihr reden konnte. Die Woche, welche ich mit dir im Juni in Arbogast verbracht habe, hatte ich nach den vielen Wochen im Labor so richtig nötig und es war schön, dich einmal wieder für längere Zeit zu sehen.

Abschließend bedanke ich mich bei meinen Eltern. Mama und Papa, ihr habt mir nicht nur mit eurer finanziellen Unterstützung dieses Studium ermöglicht, sondern viel mehr war es euer Vertrauen in mich, welches mich in den schlechteren Zeiten meines Studiums zum Weitermachen ermutigt hat.
Schön, dass es euch gibt.

DANKE!

[1] Ich habe ja deinem Papa versprochen, dich auch in der Danksagug zu erwähnen.